Monthly Notices of the ROYAL ASTRONOMICAL SOCIETY

MNRAS **437,** 2772–2789 (2014)
Advance Access publication 2013 November 27

doi:10.1093/mnras/stt2090

Empirical modelling of the BLASTPol achromatic half-wave plate for precision submillimetre polarimetry

Lorenzo Moncelsi,[1,2★] Peter A. R. Ade,[2] Francesco E. Angilè,[3] Steven J. Benton,[4] Mark J. Devlin,[3] Laura M. Fissel,[5] Natalie N. Gandilo,[5] Joshua O. Gundersen,[6] Tristan G. Matthews,[7] C. Barth Netterfield,[4,5] Giles Novak,[7] David Nutter,[2] Enzo Pascale,[2] Frédérick Poidevin,[8] Giorgio Savini,[8] Douglas Scott,[9] Juan Diego Soler,[5] Locke D. Spencer,[2,10] Matthew D. P. Truch,[3] Gregory S. Tucker[11] and Jin Zhang[2]

[1]*California Institute of Technology, 1200 E. California Blvd., Pasadena, CA 91125, USA*
[2]*Department of Physics and Astronomy, Cardiff University, 5 The Parade, Cardiff CF24 3AA, UK*
[3]*Department of Physics and Astronomy, University of Pennsylvania, 209 South 33rd Street, Philadelphia, PA 19104, USA*
[4]*Department of Physics, University of Toronto, 60 St. George Street, Toronto, ON M5S 1A7, Canada*
[5]*Department of Astronomy and Astrophysics, University of Toronto, 50 St. George Street, Toronto, ON M5S 3H4, Canada*
[6]*Department of Physics, University of Miami, 1320 Campo Sano Drive, Coral Gables, FL 33146, USA*
[7]*Department of Physics and Astronomy, Northwestern University, Evanston, IL 60208, USA*
[8]*Department of Physics and Astronomy, University College London, Gower Street, London WC1E 6BT, UK*
[9]*Department of Physics and Astronomy, University of British Columbia, 6224 Agricultural Road, Vancouver, BC V6T 1Z1, Canada*
[10]*Department of Physics and Astronomy, University of Lethbridge, 4401 University Drive, Lethbridge, Alberta T1K 3M4, Canada*
[11]*Department of Physics, Brown University, 182 Hope Street, Providence, RI 02912, USA*

Accepted 2013 October 24. Received 2013 October 22; in original form 2013 August 23

ABSTRACT

A cryogenic achromatic half-wave plate (HWP) for submillimetre astronomical polarimetry has been designed, manufactured, tested and deployed in the Balloon-borne Large-Aperture Submillimeter Telescope for Polarimetry (BLASTPol). The design is based on the five-slab Pancharatnam recipe and it works in the wavelength range 200–600 μm, making it the broadest-band HWP built to date at (sub)millimetre wavelengths. The frequency behaviour of the HWP has been fully characterized at room and cryogenic temperatures with incoherent radiation from a polarizing Fourier transform spectrometer. We develop a novel empirical model, complementary to the physical and analytical ones available in the literature, that allows us to recover the HWP Mueller matrix and phase shift as a function of frequency and extrapolated to 4 K. We show that most of the HWP non-idealities can be modelled by quantifying one wavelength-dependent parameter, the position of the HWP equivalent axes, which is then readily implemented in a map-making algorithm. We derive this parameter for a range of spectral signatures of input astronomical sources relevant to BLASTPol, and provide a benchmark example of how our method can yield improved accuracy on measurements of the polarization angle on the sky at submillimetre wavelengths.

Key words: magnetic fields – polarization – balloons – instrumentation: polarimeters – techniques: polarimetric – submillimetre: ISM.

1 INTRODUCTION

Galactic magnetic fields are believed to play a crucial role in the evolution of star-forming molecular clouds, perhaps controlling the rate at which stars are born and even determining their mass (Crutcher 2004; McKee & Ostriker 2007). However, magnetic fields are very difficult to probe on the spatial scales relevant to the star-forming processes, especially within obscured molecular clouds (e.g. Crutcher et al. 2004; Whittet et al. 2008), hence their influence on star formation has not yet been clearly established observationally.

Zeeman splitting of molecular lines, which allows a direct measurement of the strength of the line-of-sight component of the local magnetic field, has been carried out successfully for a number of molecular cloud cores (e.g. Crutcher et al. 1999), though the technique is difficult and limited to the brightest of regions (Crutcher 2012). A promising alternative method is to observe clouds with a

★E-mail: moncelsi@caltech.edu

far-infrared/submillimetre (FIR/submm) polarimeter (e.g. Hildebrand, Dragovan & Novak 1984; Hildebrand et al. 2000; Ward-Thompson et al. 2000). By tracing the linearly polarized thermal emission from aspherical dust grains aligned with respect to the local magnetic fields, we can estimate the direction of the plane-of-the-sky component of the field within the cloud (Davis & Greenstein 1951; Dolginov & Mitrofanov 1976; Lazarian 2007), and its strength via the Chandrasekhar & Fermi (1953) technique, provided that ancillary measurements of the turbulent motion velocity are available. The observed morphology in submm polarization maps can also be used, in synergy with magnetohydrodynamic simulations, to study the imprint of turbulence and magnetization on the formation of structure in the cloud (Houde et al. 2009; Soler et al. 2013).

Ground-based observations with the Submillimetre Common-User Bolometer Array (SCUBA) polarimeter (Murray et al. 1997; Greaves et al. 2003) and the Submillimeter Polarimeter for Antarctic Remote Observations (SPARO; Novak et al. 2003) show that the submm emission from prestellar cores and giant molecular clouds (GMCs) is indeed polarized to a few per cent (Ward-Thompson et al. 2000; Li et al. 2006). *Planck* (Ade et al. 2011) will provide coarse resolution (∼5 arcmin) submm polarimetry maps of the entire Galaxy. The Atacama Large Millimeter/submillimeter Array (ALMA; Wootten & Thompson 2009) will provide sub-arcsecond millimetre (mm) and submm polarimetry, capable of resolving fields within cores and circumstellar discs, but will not be sensitive to cloud-scale fields.

The Balloon-borne Large-Aperture Submillimeter Telescope for Polarimetry (BLASTPol; Marsden et al. 2008; Fissel et al. 2010; Pascale et al. 2012), with its arcminute resolution, is the first submm polarimeter to map the large-scale magnetic fields within molecular clouds with unique combined sensitivity and mapping speed, and sufficient angular resolution to observe into the dense cores. BLASTPol will be able to trace magnetic structures in the cold interstellar medium from scales of 0.05 pc out to 5 pc, thus providing a much needed bridge between the large area but coarse-resolution polarimetry provided by *Planck* and the high resolution but limited field-of-view maps of ALMA.

BLASTPol successfully completed two science flights over Antarctica during the austral summers of 2010 and 2012, mapping the polarized dust emission at 250, 350 and 500 μm over a wide range of column densities corresponding to $A_V \gtrsim 4$ mag, yielding hundreds to thousands of independent polarization pseudo-vectors per cloud, for a dozen between GMCs and dark clouds. The first scientific results from the 2010 campaign are soon to be released (Matthews et al. 2013; Poidevin et al., in preparation), while the 2012 data are still under analysis (an overview of the 2012 observations can be found in Angilè et al. in preparation).

The BLASTPol linear polarization modulation scheme comprises a stepped cryogenic achromatic half-wave plate (HWP) and photolithographed polarizing grids placed in front of the detector arrays, acting as analysers. The grids are patterned to alternate the polarization angle sampled by 90° from bolometer-to-bolometer along the scan direction. BLASTPol scans so that a source on the sky passes along a row of detectors, and thus the time required to measure one Stokes parameter (either Q or U) is just equal to the separation between bolometers divided by the scan speed. During operations, we carry out spatial scans at four HWP rotation angles spanning 90° (22°.5 steps), allowing us to measure the other Stokes parameter through polarization rotation.

The use of a continuously rotating or stepped HWP as a polarization modulator is a widespread technique at (sub)mm wavelengths (e.g. Renbarger et al. 2004; Hanany et al. 2005; Pisano et al. 2006; Savini, Pisano & Ade 2006; Savini et al. 2009; Johnson et al. 2007; Li et al. 2008; Matsumura et al. 2009). A thorough account of the HWP non-idealities and its inherent polarization systematics, especially for very achromatic designs, has become necessary as the accuracy and sensitivity of (sub)mm instruments have soared in recent years.

The literature offers numerous efforts to address, through simulations, the impact of the inevitable instrumental systematic errors due to the polarization modulation strategy in the unbiased recovery of the Stokes parameters Q, U on the sky, especially for cosmic microwave background (CMB) polarization experiments (e.g. O'Dea, Challinor & Johnson 2007; Brown et al. 2009; O'Dea et al. 2011). In addition, physical and analytical models have been developed to retrieve the frequency-dependent modulation function of achromatic HWPs and estimate the corrections due to non-flat source spectral indices (Savini et al. 2006, 2009; Matsumura et al. 2009).

Nevertheless, little work has been published on incorporating the *measured* HWP non-idealities in a data-analysis pipeline and ultimately in a map-making algorithm. Bryan, Montroy & Ruhl (2010a) derive an analytic model that parametrizes the frequency-dependent non-idealities of a monochromatic HWP and present a map-making algorithm that accounts for these. Bao et al. (2012) carefully simulate the impact of the spectral dependence of the polarization modulation induced by an achromatic HWP on measurements of the CMB polarization in the presence of astrophysical foregrounds, such as Galactic dust. However, both these works assume the nominal design values for the build parameters of the HWP plus anti-reflection coating (ARC) assembly.

While this assumption is a reasonable one when no spectral measurements of the HWP as-built are available, several studies clearly show that the complex multislab crystal HWP and its typically multilayer ARC are practically impossible to manufacture *exactly* to the desired specifications. In particular, Savini et al. (2006, 2009) and Pisano et al. (2006) caution against the finite precision to which the multiple crystal substrates composing an achromatic HWP can be aligned relative to each other in the Pancharatnam (1955) scheme. In addition, Zhang et al. (2009) show how some of the design parameters in the ARC can slightly change during the bonding of layers, achieved via a hot-pressing technique (Ade et al. 2006). We will briefly cover these points and discuss the repercussions on the HWP performance.

This work describes a novel empirical method that allows the reconstruction of the Mueller matrix[1] of a generic HWP as a function of frequency through spectral transmission measurements of the HWP rotated by different angles with respect to the input polarized light. Not only does this method give complete and quantitative information on the *measured* spectral performance of the HWP, but it also provides a direct avenue to accounting for the non-idealities of the HWP *as-built* in a map-making algorithm. This empirical approach is applied to the BLASTPol HWP and will help improve the accuracy on astronomical measurements of polarization angles at submm wavelengths.

The layout of this paper is as follows. In Section 2, we give an overview of the manufacturing process for BLASTPol's five-slab sapphire HWP. Section 3 describes the spectral measurements, while Section 4 presents the empirical model as well as the main

[1] We adopt the Stokes (1852) formalism to represent the time-averaged polarization state of electromagnetic radiation; for a review of polarization basics we refer the reader to Collett (1993).

results of the paper. Finally, in Section 5, we describe the algorithm for the naive-binning map-making technique implemented by BLASTPol, which naturally accounts for the *measured* HWP non-idealities. Section 6 contains our conclusions.

2 THE BLASTPoL HALF-WAVE PLATE

Wave plates (or retarders) are optical elements used to change the polarization state of an incident wave, by inducing a pre-determined phase difference between two perpendicular polarization components. A (monochromatic) wave plate can be simply obtained with a single slab of uniaxial birefringent crystal of specific thickness, which depends upon the wavelength and the index of refraction of the crystal. A birefringent crystal is characterized by four parameters, n_e, n_o, α_e, α_o, the real part of the indices of refraction and the absorption coefficient (in cm^{-1}) for the extraordinary and ordinary axes of the crystal. At a specific wavelength λ_0, the phase shift induced by a slab is determined uniquely by its thickness d, and reads:

$$\Delta\varphi(\lambda_0) = \frac{2\pi d}{\lambda_0}(n_e - n_o). \quad (1)$$

Given the operating wavelength λ_0, the required phase shift for the wave plate is achieved by tuning the thickness d.

While monochromatic wave plates have been (and are still being) used in (sub)mm astronomical polarimeters (see e.g. Renbarger et al. 2004; Li et al. 2008; Bryan et al. 2010a,b; Dowell et al. 2010), the inherent dependence of the phase shift on wavelength, expressed in equation (1), constitutes an intrinsic limit in designing a polarization modulator that operates in a broad spectral range (i.e. achromatic).

2.1 Achromatic HWP design

Achromaticity is necessary for wave plates that are designed for use with multiband bolometric receivers, such as BLASTPol, PILOT (Bernard et al. 2007) or SCUBA-2 (Bastien et al. 2005; Savini et al. 2009). To achieve a broad-band performance, multiple-slab solutions have been conceived in the past (Pancharatnam 1955; Title & Rosenberg 1981) to compensate and keep the phase shift approximately constant across the bandwidth, by stacking an odd number (usually three or five) of birefringent substrates of the same material, which are rotated with respect to each other about their optical[2] axes by a frequency-dependent set of angles.

Achromatic wave plates have been designed and built for astronomical polarimeters at (sub)mm wavelengths by many authors in the past decade (Hanany et al. 2005; Pisano et al. 2006; Savini et al. 2006, 2009; Matsumura et al. 2009), following the Poincaré sphere (PS) method first introduced by Pancharatnam (1955). Because the four parameters that characterize a crystal, n_e, n_o, α_e, α_o, all depend upon wavelength (in particular, the different frequency dependence of the ordinary and extraordinary refraction indices enters equation (1) in a non-trivial way, as we will illustrate in detail for sapphire), the design of an achromatic HWP becomes progressively more difficult as the bandwidth increases.

Using the PS method, we have designed an HWP for the BLASTPol instrument, which requires an extended frequency range to cover three adjacent 30 per cent wide spectral bands at 250, 350 and 500 μm. A Pancharatnam (1955) five-slab design is chosen with axis orientations of $\Phi_0 = 0°$, $\Phi_1 = 26°$, $\Phi_2 = 90°.3$, $\Phi_1 = 26°$ and $\Phi_0 = 0°$; these angles are optimized using the physical and analytical model developed by Savini et al. (2006) for an achromatic HWP, which in turn is based on the work of Kennaugh & Adachi (1960). In Fig. 1, we show an exploded view of the HWP assembly; to our knowledge, with its ∼100 per cent bandwidth, this is the broadest band HWP manufactured to date at (sub)mm wavelengths for which measurements are published.[3]

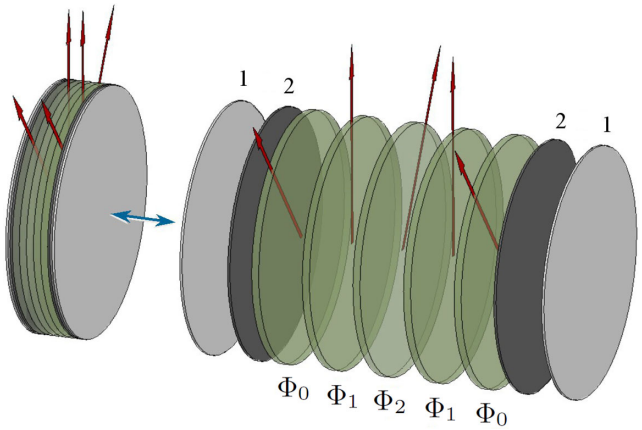

Figure 1. Exploded view of the BLASTPol HWP. We also show the two-layer antireflection coating described in Section 2.2 (figure modified from Savini et al. 2006).

2.2 HWP manufacture

In addition to the broad spectral range of operation, the BLASTPol HWP is required to function at cryogenic temperatures (4 K; see Fissel et al. 2010) for two main reasons: (1) reduce the thermal emission from a warm element placed in the optical path, which would constitute a significant background load on the bolometers and (2) reduce the losses in transmission due to absorption from the stack of five crystal substrates, which drops dramatically with temperature. The absorption in a crystal at FIR wavelengths is the result of the interactive coupling between the incident radiation and phonons – the thermally induced vibrations of the constituent atoms of the substrate crystal lattice. Because the phonon population is much reduced at low temperatures, cooling the crystal effectively reduces the absorption.

The two obvious candidates (uniaxial birefringent) crystals are sapphire and quartz, because of their favourable optical properties in the FIR/submm. Sapphire is chosen over quartz due to its larger difference between ordinary and extraordinary refraction indices ($\Delta n_{e\text{-}o} \approx 0.32$ for sapphire, and ≈0.032 for quartz; Loewenstein, Smith & Morgan 1973), which implies a smaller thickness for the substrates (see equation 1). Since quartz and sapphire have a comparable level of absorption at cryogenic temperatures in the wavelength range of 200–600 μm (Loewenstein et al. 1973), thinner

[2] We distinguish between 'optic' axis of a crystal, i.e. the direction in which a ray of transmitted light experiences no birefringence, and 'optical' axis, i.e. the imaginary line along which there is some degree of rotational symmetry in the optical system.

[3] The HWP designed for the mm-wave E and B EXperiment (EBEX; Matsumura et al. 2009; Reichborn-Kjennerud et al. 2010) is nominally slightly more achromatic, with an ∼110 per cent bandwidth. However, a comprehensive spectral characterization of the final (as-flown) AR-coated HWP assembly has yet to be published.

substrates are desirable to minimize absorption losses. Nonetheless, the thin sapphire substrates chosen for the BLASTPol HWP do indeed show appreciable absorption, especially at the shortest wavelengths (250 μm band; see Section 3).

The five slabs of the Pancharatnam (1955) design all have the same thickness. To cover the broad wavelength range of 200–600 μm, a substrate thickness is chosen to produce an HWP at the central wavelength of the central band, 350 μm. By using the values of the refractive indices for cold sapphire published by Loewenstein et al. (1973) and Cook & Perkowitz (1985, $\Delta n_{\mathrm{e-o}}^{350\,\mu\mathrm{m}} \approx 0.32$), and imposing the required phase shift of 180° between the two orthogonal polarizations travelling through the plate, equation (1) yields for the thickness of a single substrate a value ∼0.547 mm. The nearest available thickness on the market is 0.5 mm, and sapphire cannot be easily ground to the desired thickness due to its brittleness. A deviation of ∼0.047 mm from the desired thickness would naively translate into a departure of up to ∼15° from the ideal phase shift of 180° at 350 μm. However, the case of a multislab Pancharatnam HWP is more complex, since the phase shift becomes an 'effective' one and requires proper modelling as a function of frequency, which we have included in Section 4.3.

The orientation of the optic axis on each sapphire substrate is determined with a polarizing Fourier transform spectrometer (pFTS hereafter), which is briefly described in Section 3.1. Each substrate is rotated between two aligned polarizers at the pFTS output until a maximum signal is achieved. The use of two polarizers avoids any complication from a partially polarized detecting system and any cross-polarization incurred from the pFTS output mirrors. The HWP is assembled by marking the side of each substrate with its reference optic axis and rotating each element according to the Pancharatnam design described in the previous section. The stack of five carefully oriented sapphire substrates, interspersed with 6 μm layers of polyethylene, are bonded together with a hot-pressing technique used in standard FIR/submm filter production (Ade et al. 2006). The polyethylene has negligible effects on the final optical performance of the HWP, because when heated it seeps into the roughened surfaces of the adjacent substrates.

In order to improve the robustness of the bond, the individual substrates are sandblasted with aluminium oxide (Al_2O_3) prior to fusion; this procedure dramatically improves the grip of the polyethylene between adjacent crystal surfaces. Careful cleansing and degreasing of all the crystal surfaces is required after sandblasting; in particular, we found trichloroethylene to be most effective in removing the traces of oily substances due to the sandblasting process.

A two-layer broad-band ARC, necessary to maximize the in-band transmission of the HWP, is also hot-pressed to the front and back surfaces of the assembled plate, again using 6 μm layers of polyethylene. The layer adjacent to the sapphire is an artificial dielectric metamaterial (ADM) composed of metal-mesh patterned on to polypropylene sheets (Zhang et al. 2009), while the outer layer is a thin film of porous polytetrafluoroethylene (PTFE). The thickness of the final stack (coated HWP) is 2.80 ± 0.01 mm. The diameter of the ARC is set to 88.0 ± 0.1 mm, slightly smaller than that of the HWP (100.0 ± 0.1 mm) to avoid any contact between the coating and the HWP mount (see Fissel et al. 2010); the ARC is bonded concentrically to the HWP and thus its diameter defines the optically active area of the HWP.

Because of the thermal expansion mismatch between the sapphire and the polypropylene, the HWP assembly has been cryogenically cycled numerous times prior to the flight to test the robustness of the bond at liquid helium temperatures. The HWP has been successfully installed in the BLASTPol cryogenic receiver and has been flown twice from a balloon platform, without delamination of the ARC or damage to the assembly.

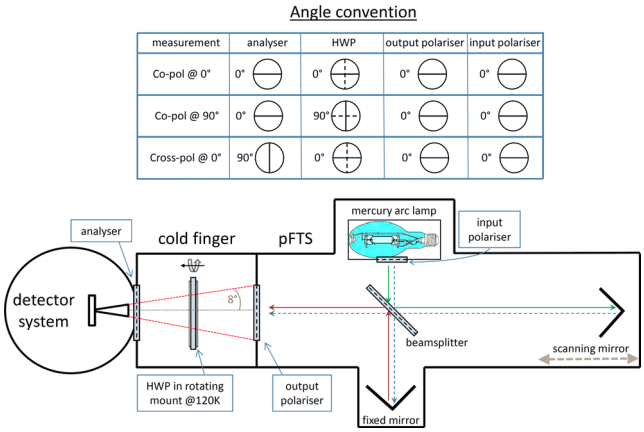

Figure 2. Schematic drawing of the spectral measurements setup. The $f/3.5$ horizontally polarized output of a pFTS illuminates the HWP with an ∼8° incidence angle and is focused directly on to the horn aperture of the bolometric detector. The analyser alternatively parallel or perpendicular to the pFTS output polarizer creates the necessary polarization selection for the 'co-pol' and 'cross-pol' sets of measurements, as depicted in the table above. The lines in the circles indicate the selected polarization, so that for the photolithographed polarizers the wire grid orientation is perpendicular to the lines.

However, for cryogenic crystal HWPs much larger than the BLASTPol one, the application of a metal-mesh ADM as an ARC has proven extremely challenging. Therefore, extending previous work by Pisano et al. (2008), we have recently designed and realized a prototype polypropylene-embedded metal-mesh broad-band achromatic HWP for mm wavelengths (Zhang et al. 2011); this will allow next-generation experiments with large-aperture detector arrays to be equipped with large-format ($\gtrsim$20 cm in diameter) HWPs for broad-band polarization modulation.

3 SPECTRAL CHARACTERIZATION

The first step to retrieving the frequency-dependent Mueller matrix and phase shift of the BLASTPol HWP is to measure its transmission as a function of frequency and incoming polarization state. Because of the strong dependence of the sapphire absorption coefficient on temperature, we cannot limit ourselves to determining the room-temperature response of the HWP, which is designed to operate at cryogenic temperatures. Therefore, we measure its spectral response in a vacuum cavity, cooled to temperatures as low as currently possible with our experimental apparatus (∼120 K).[4]

3.1 Experimental setup

We fully characterize the spectral performance of the BLASTPol HWP by using a pFTS of the Martin-Puplett (1970) type. A schematic drawing of the experimental setup is shown in Fig. 2; in the following, we describe each element in sequential order from the source to the detector system.

[4] Room-temperature spectra were acquired and can be made available to the reader, but are neither reported here nor used in the subsequent analysis, because plagued by significant in-band transmission loss due to the absorption from sapphire.

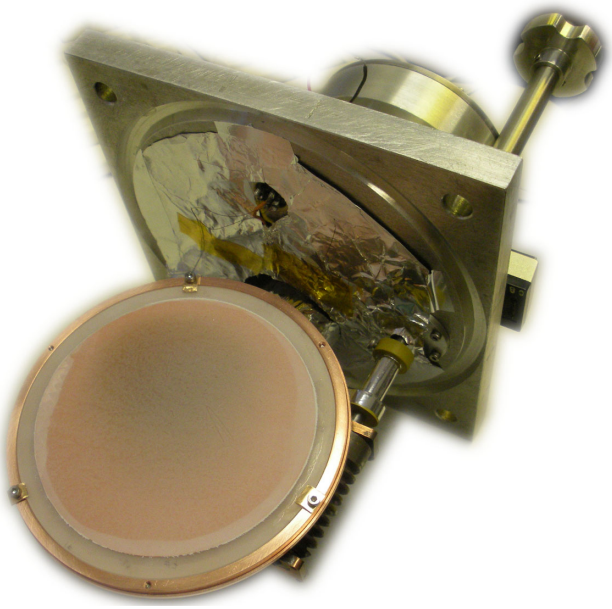

Figure 3. Photograph of the 'cold finger' module, which fits in the vacuum cavity at the output port of the pFTS. The central cylinder is hollow and has to be regularly replenished with liquid nitrogen to maintain the temperature of the HWP at ∼120 K. Aluminium insulation and a thick copper strap improve the thermal performance of the module. Two thermometers monitor the temperature at the bottom of the cylinder (base plate) at the edge of the copper HWP holder. The rotator is manually driven via a gear train and a vacuum-seal shaft leading to a manual knob outside the module. The resolution of the analogue encoder on the rotation angle is 0.°06. The presence of a thermometer on the rotating element prevents rotations greater than ∼180°.

The source is an incoherent mercury arc lamp with an aperture of 10 mm, whose emission is well approximated by a blackbody spectrum at $T_{\rm eff} \approx 2000$ K; a low-pass filter blocks radiation from the source at wavelengths shorter than ∼3.4 μm. The interferometer is equipped with a P1[5] beam divider, a P2 input polarizer (at the source) and a P10 output polarizer. The pFTS has a (horizontally) polarized output focused beam with $f/3.5$ or, in other words, a converging beam with angles $\theta \lesssim 8^\circ$.

This beam spread is conveniently close to the ∼5.°7 incidence angle that the HWP is illuminated by in the $f/5$ BLASTPol optics box (see Fissel et al. 2010; Pascale et al. 2012), therefore it is ideal optically to place the HWP between the pFTS output polarizer and the detector system the beam focuses on to, without the need for additional optical elements; this also ensures an even illumination of the entire HWP optically active area.

We position the HWP in a liquid nitrogen-cooled removable module retrofitted in the vacuum cavity at the output port of the pFTS; a photograph and a brief description of the module, which we refer to as 'cold finger', are given in Fig. 3. The manually driven rotating mount can rotate the HWP about its optical axis to obtain the polarization modulation, with a resolution on the rotation angle of 0.°06.

The HWP is placed centrally between the pFTS output polarizer and a P10 analyser, installed at the exit port of the vacuum cavity; the efficiency of these polarizers is separately determined to exceed 99.8 per cent over the range of frequencies of interest, with a cross-polarization of less than 0.1 per cent. The polarizers are initially aligned with respect to each other, with the grid wires vertical (thus selecting horizontal polarization) with respect to the optical bench.

A small cryostat, connected with no air gaps to the exit port of the vacuum cavity, houses a feedhorn-coupled composite bolometer cooled to 1.5 K by pumping on the liquid helium bath. The spectral coverage of the data is thus defined by the cut-off frequency of the light collector waveguide (5 cm^{-1}) and by a low-pass filter (60 cm^{-1}) installed in the cryostat to minimize photon noise.

Finally, the rapid-scan system records interferograms with an 8 μm sampling interval over a 10 cm optical path difference, at a scan speed of 2 cm s^{-1}; this results in a Nyquist frequency of 625 cm^{-1} and a spectral resolution of 0.05 cm^{-1}.

3.2 Measurement strategy and results

After the roughly two hours needed for the cold finger module to thermalize, its base plate reaches temperatures close to 77 K, while the HWP holder thermalizes at about 120 K, despite the thermal insulation and high thermal conductivity link to the base plate. Other cryogenic tests conducted by bonding a thermometer at the centre of a single slab of sapphire ensure that the temperature measured at the edge of an aluminium or copper holder closely matches that of the sapphire substrate at its centre. While maintaining a constant level of liquid nitrogen in the cold finger, we can characterize the spectral response of the cold HWP, by rotating it inside the vacuum cavity.

Following the convention depicted in Fig. 2, measurements with aligned polarizers are referred to as 'co-pol' transmission, $T_{\rm cp}$. The HWP has a complementary response when the analyser is rotated by 90° about the optical axis of the system (i.e. horizontal wires, selecting vertical polarization); data taken with this configuration are necessary to completely characterize the HWP, and are referred to as 'cross-pol' transmission,[6] $T_{\rm xp}$.

The very first data set, which we refer to as the background spectrum, must be obtained in co-pol configuration by scanning the spectrometer in the absence of the HWP. This data set defines the pFTS reference spectral envelope, and it is the set against which all the following spectra are divided in order to account for the spectral features of the source, pFTS optics and detector system. Subsequently, the HWP is inserted in between the polarizers in co-pol configuration, and spectra are acquired at many different HWP rotation angles (resulting in a data cube). To enhance the spectral signal-to-noise ratio, each data set at a given angle is obtained by computing the Fourier transform of an (apodized and phase-corrected) average of 60 interferograms with the mirror scanned in both the forward and backward directions. As anticipated, the resulting spectra are divided by the background data set, which in turn is the average of three spectra, to obtain the transmission of the coated HWP alone as a function of frequency.

Over two days of measurements, we acquire data cubes for co-pol and cross-pol transmissions, shown, respectively, in Figs 4 and 5, where we only display spectra taken at rotation angles near the HWP maxima and minima, for visual clarity. The full data sets,

[5] The notation Pn refers to a wire grid polarizer that has a grid period of n [μm], with $n/2$ copper strips and $n/2$ gaps, photolithographed on a 1.5 μm mylar substrate.

[6] We note that this definition of cross-pol may differ from other conventions adopted in the literature (e.g. that of Masi et al. 2006, who operate without an HWP).

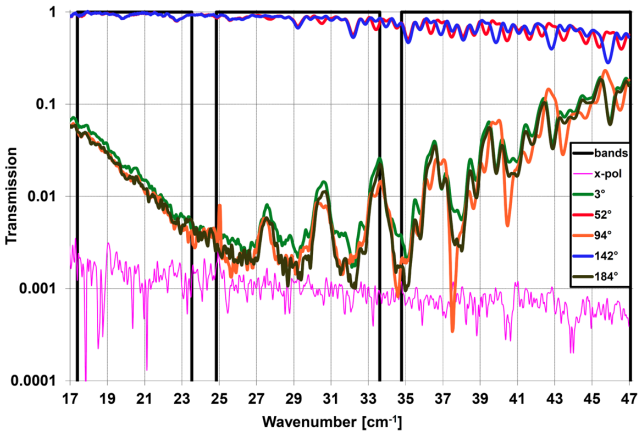

Figure 4. Measured co-pol transmission spectra of the coated BLASTPol HWP cooled to ∼120 K. Each line is obtained at a different HWP rotation angle by computing the Fourier transform of an (apodized and phase-corrected) average of 60 interferograms. For visual clarity, we only show here spectra at rotation angles near the HWP maxima and minima, omitting data taken at intermediate angles (shown in Fig. 6). The solid vertical black lines show the approximate extent of the three BLASTPol bands.

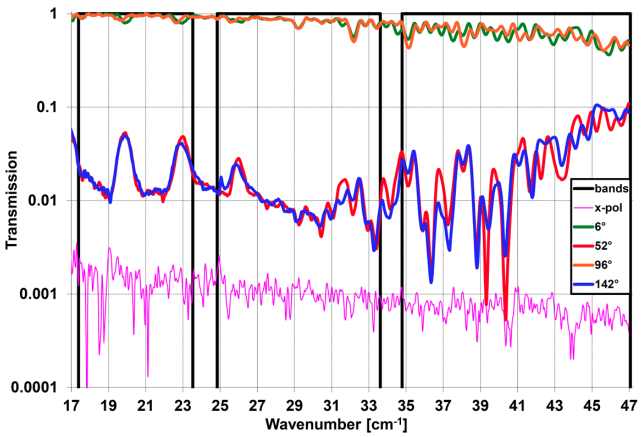

Figure 5. Measured spectra of the HWP cooled to ∼120 K equivalent to those shown in Fig. 4 but for cross-pol transmission.

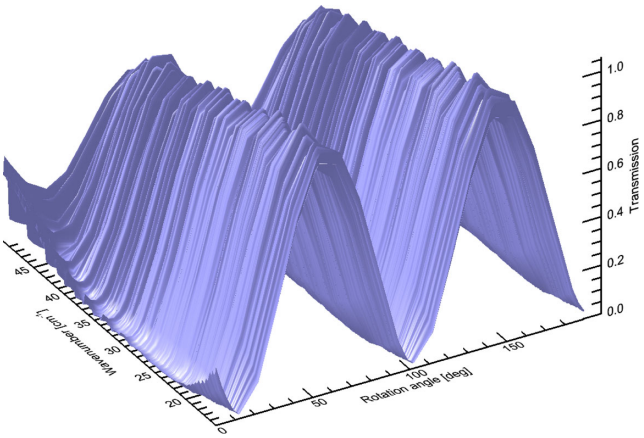

Figure 6. Data cube represented by a surface obtained by stacking a set of spectral co-pol transmissions of the HWP at different angles. Each measured spectra is a slice of the surface perpendicular to the angle axis.

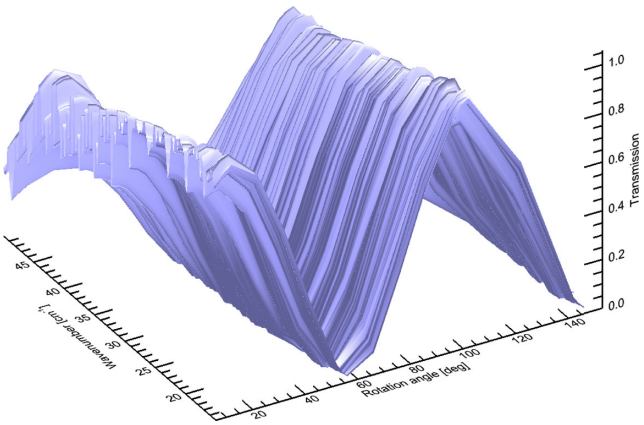

Figure 7. Equivalent data cube to that shown in Fig. 6 but for cross-pol transmission. Note how the two surfaces are complementarily in counter-phase to each other. Each measured spectra is a slice of the surface perpendicular to the angle axis.

including spectra taken at intermediate angles (roughly every 10° between 0° and ∼180°), are shown in Figs 6 and 7 as 3D surfaces.

Because of the controlled environment in the vacuum cavity, our measurements are not susceptible to changes in the external environment; however, we repeat background scans at the very end of our measurement session to monitor drifts in the bolometer responsivity and other potential systematic effects. Prior to inserting the HWP in the cavity, we have also characterized the instrumental cross-pol of this setup by rotating the analyser by 90° in cross-pol configuration and acquiring three spectra. By averaging these cross-pol spectra and dividing by the co-pol background, we measure a cross-pol level of 0.2 per cent or less across the entire spectral range of interest (5–60 cm^{-1}); we include the resulting cross-pol spectrum in Figs 4 and 5 (dark pink line).

An ideal HWP modulates the polarization at 4θ, therefore in a complete revolution there are four maxima (and minima), two for each of the birefringent axes. The (arbitrary) zero angle in Figs 4–7 does not (need to) coincide with an HWP maximum (minimum), which is the HWP angle at which we measure maximum (minimum) total power on the detector; this of course includes signal outside of the HWP bands (in the range 5–60 cm^{-1}). As we show in Section 4.2, the position of the equivalent axes of the sapphire plate stack (and hence the position of the HWP maxima/minima) depends upon the wavelength. Therefore, the HWP maxima (and minima) we assign while taking spectra are just rough approximations. Although we increase the angle sampling rate in the vicinities of a maximum or minimum (with steps of 3° rather than 10°), in order to fully characterize the HWP it is not necessary to take spectra *exactly* at its maxima or minima.

We verify that the experimental setup is symmetric with respect to the HWP rotation and that there are no artefacts arising from misalignments in the optical setup by measuring no appreciable change in pairs of data sets taken at angles that are exactly 180° apart, due to polarization symmetry.

In the surfaces depicted in Figs 6 and 7, slices of the data cube along the wavenumber axis constitute the measured spectra at different HWP angles, while slices along the angle axis represent the modulation function of the HWP at a given frequency or, more precisely, within a narrow band of frequencies defined by a combination of spectral resolution and the spectrometer's instrument response function.

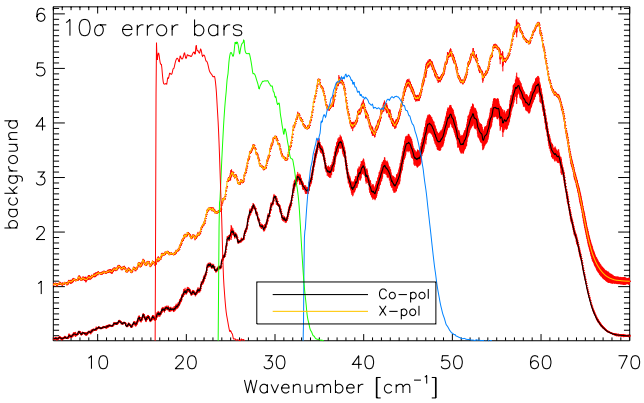

Figure 8. Noise estimation for the spectra shown in Figs 4 and 5. We plot the mean background spectra (in arbitrary units) for the co-pol (black solid line) and cross-pol (yellow solid line, shifted by 1 in the positive y direction for visual clarity) as a function of wavenumber. The (10σ) error bars (in red) are quantified as the statistical error on the mean. Also shown for reference is the relative spectral response of the three BLASTPol channels, in arbitrary units. Henceforth, we adopt a colour code in the plots whereby curves referring to the three BLASTPol bands, 250, 350 and 500 μm are drawn in blue, green and red, respectively.

The features visible in all spectra are spectral fringes due to standing waves generated inside the stack of dielectric substrates (even with a quasi-perfect impedance matching coating on the outer surfaces); the presence of several interspersed layers of polyethylene enhances the amplitude of the fringes by introducing small amounts of absorption at every internal reflection.

3.3 Uncertainties on the measured spectra

Because we average 60 interferograms to obtain the final spectrum at each HWP position, the statistical uncertainty associated with the average on a single data set is found to be negligible, as expected. Rather, we decide to average together all the available background interferograms that are collected over one day of measurements, and take their statistical dispersion as our estimate of the uncertainty associated with all the spectra collected on that day. Because the thermodynamic conditions in the cavity under vacuum are not susceptible to changes in the external environment, this procedure allows us to account for drifts in the bolometer responsivity and other potential systematic effects. We report in Fig. 8 the mean background spectra and the associated error (shown as 10σ error bars for visual clarity) for the co-pol and cross-pol measurement sessions. These errors (1σ) are used in Section 4 to estimate the uncertainties on the HWP Mueller matrix coefficients.

3.4 Comparison with design parameters

While the major goal of this work is to provide an avenue for including the measured non-idealities of the BLASTPol HWP *as-built* in a map-making algorithm, it is useful at this stage to compare the nominal values of the build parameters we assumed to design the HWP with the actual values that can be estimated via the physical and analytical model developed by Savini et al. (2006, 2009, which we refer to for a complete account of the formalism and implementation).

In this work, the physical model is fit to the spectral data described in Section 3.2 by allowing the HWP build parameters to vary in a physical way around the nominal values. We report in Fig. 9, a comparison between the measured co-pol transmission spectra near the HWP maxima/minima and the corresponding physical model, whose best-fitting parameters are listed in Table 1, along with the nominal ones.

Among all the parameters presented in Table 1, let us focus on the angles at which the sapphire substrates are oriented, Φ_i ($i = 1, \ldots, 4$; see Section 2.2), since they have a greater impact on what follows. The best-fitting orientation angles are up to 3–4°

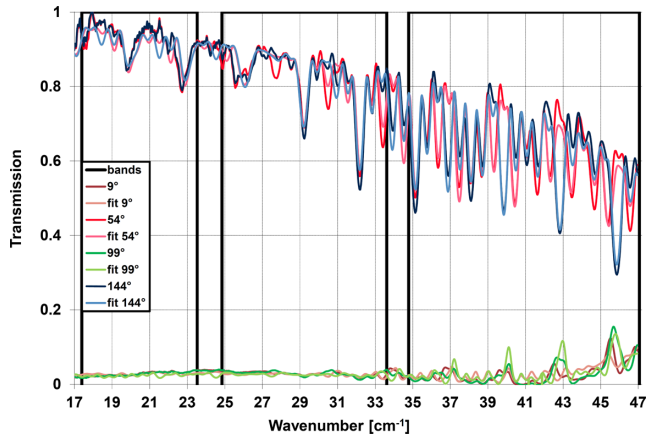

Figure 9. Comparison between the measured co-pol transmission spectra near the HWP maxima/minima and the corresponding physical model of Savini et al. (2006), which is fit to the data by allowing the build parameters of the HWP (refraction index and thickness of all the materials, orientation of the birefringent substrates) to vary in a physical way around the nominal values.

Table 1. Best-fitting build parameters of the BLASTPol HWP estimated using the physical model of Savini et al. (2006). $n^0_{e(o)}$ and $n^1_{e(o)}$ are, respectively, the constant and linear terms of the refraction index for the sapphire (extra)ordinary axis, modelled with a linear dependence on wavenumber; d is the thickness of the sapphire substrates; $t_{\rm PE}$ is the thickness of the polyethylene layers; Φ_i ($i = 1, \ldots, 4$) are the four angles at which the sapphire substrates are oriented (assuming $\Phi_0 = 0°$); $n^i_{\rm ARC}$ and $t^i_{\rm ARC}$ ($i = 1, 2, 3$) are, respectively, the refraction indices and the thicknesses of the ith layer of ARC (in order of penetration into the HWP), which is modelled as series of equivalent dielectrics.

Parameter	Units	Nominal	Best fit	Uncertainty
n^0_o		3.052[a]	3.065	0.002
n^1_o	cm		0.002 07	0.000 08
n^0_e		3.372[a]	3.444	0.001
n^1_e	cm		0.001 27	0.000 08
d	μm	500.0	490.4	0.5
$t_{\rm PE}$	μm	6.0	3.5	0.5
Φ_1	deg	26	22	1
Φ_2	deg	90.3	87	1
Φ_3	deg	26	23	1
Φ_4	deg	0	−1	1
$n^1_{\rm ARC}$		1.375[b]	1.26	0.01
$t^1_{\rm ARC}$	μm	54	72	2
$n^2_{\rm ARC}$			1.62	0.01
$t^2_{\rm ARC}$	μm		37	3
$n^3_{\rm ARC}$			2.28	0.01
$t^3_{\rm ARC}$	μm		36	2

[a] Loewenstein et al. (1973); [b] PTFE Zhang et al. (2009).

smaller than the design goal. While this is not surprising given the practical challenge of keeping a stack of five plates (interspersed with thin slippery layers of polyethylene) aligned to within ∼3 mm (linear length of a 3°.5 arc for a 100 mm diameter), such a deviation from the desired values will affect the HWP performance, and in particular its phase shift as a function of frequency.

In the following sections, we present all the HWP performance parameters, for which the physical model presented in this section is verified to be in general agreement with the empirical model we develop in Section 4. However, we will show in Section 4.3 that the empirical model is inadequate to retrieve the HWP phase shift and we will have to resort to the physical model again to compare the design and best-fitting phase shift versus frequency. This will give us a chance to expand more on which performance parameters are more directly affected by plate alignment errors.

3.5 Modulation function and efficiency

We can reduce the dependence on frequency of our data cubes by integrating over the spectral bands of BLASTPol, as follows:

$$\overline{T}^{\rm ch}_{\rm cp}(\theta) = \frac{\int_0^\infty \Sigma^{\rm ch}(\nu)\, T_{\rm cp}(\theta,\nu)\, {\rm d}\nu}{\int_0^\infty \Sigma^{\rm ch}(\nu)\, {\rm d}\nu}. \quad (2)$$

Here the superscript 'ch' refers to one among 250, 350 and 500 μm, $\Sigma^{\rm ch}(\nu)$ is the measured spectral response of each of the BLASTPol bands (see Pascale et al. 2008), and $T_{\rm cp}(\theta,\nu)$ are points on the co-pol surface depicted in Fig. 6. A similar expression can be written for the cross-pol band-integrated transmission. By performing this integration at every angle for which spectral data have been obtained, the interpolation of these data points will result in the modulation functions of the HWP at ∼120 K for each of the BLASTPol bands; these curves are shown in Figs 10 (co-pol) and 11 (cross-pol).

The modulation curves presented here are valid for input sources that have a flat spectrum in the BLASTPol bands. Equation (2) can be generalized to include the known (or assumed) spectral signature of a given astronomical or calibration source (see also e.g. Novak et al. 1989, equation 2). More generally, all the band-averaged quantities that we have defined here and will be defined in the following are potentially affected by the spectral shape of the input source. However, we will see how the HWP transmission and modulation efficiency are very weakly dependent on the spectral index of the input source, whereas the position of the equivalent axes of the sapphire plate stack is more significantly affected (see also the analysis carried out by Savini et al. 2009), especially at 250 and 500 μm.

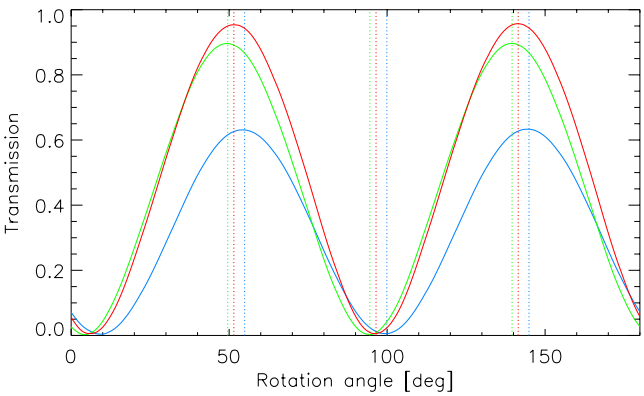

Figure 10. Band-integrated co-pol modulation functions of the BLASTPol HWP at ∼120 K. The curves show the HWP polarization modulation functions for a fully polarized source (with a flat spectrum) parallel to the analyser in the three spectral bands. Note how the positions of the maxima (and minima) depend on the wavelength, even when considering a flat-spectrum polarized input source; the dotted vertical lines show the band-integrated positions of the HWP extrema (shown in Fig. 16), which result from the fitting routine described in the next sections.

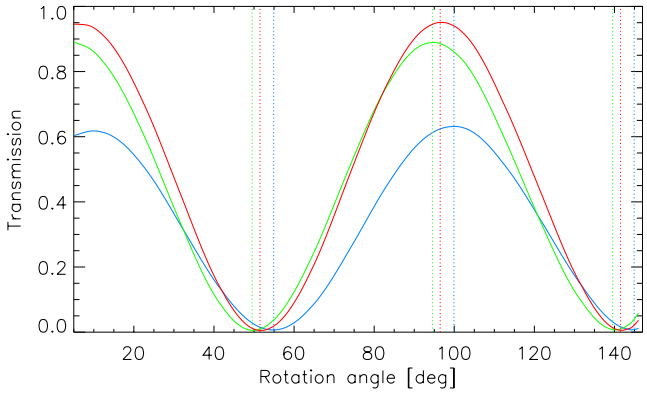

Figure 11. Band-integrated modulation functions equivalent to those shown in Fig. 10 but for cross-pol transmission.

Figs 10 and 11 clearly show that there is a significant dependence of the position of the HWP maxima and minima upon frequency, even when considering a flat-spectrum polarized input source. These effects are particularly important for an 'HWP step and integrate' experiment such as BLASTPol, and a polarization calibration must be performed by using information from the characterization of the HWP. We begin to tackle this problem in the next section, where we outline a relatively simple solution to account for most of the HWP non-idealities in the data-analysis pipeline, and in particular in the map-making algorithm (see Section 5).

The spectral transmission data sets of the HWP cooled to ∼120 K, when compared to those taken with the HWP at room temperature (not reported here for brevity), show a definite abatement of the in-band losses due to absorption from sapphire, as expected. However, the effect is still appreciable, especially above ∼25 cm^{-1}. As we will show in the following, we have evidence that the residual absorption nearly vanishes when the sapphire is further cooled to 4 K, as it is when the HWP is installed in the BLASTPol cryostat. While it is not currently feasible for us to measure the spectral response of the HWP cooled to 4 K, the unique quality and completeness of our data set allow us to fully characterize the performance of the BLASTPol HWP.

We extrapolate our 'cold' data set to 4 K, using the analytical relations shown in Fig. 12.[7] The HWP modulation efficiency is defined as $(T^{0^\circ}_{\rm cp} - T^{0^\circ}_{\rm xp})/(T^{0^\circ}_{\rm cp} + T^{0^\circ}_{\rm xp})$, where the 'co-pol' and 'cross-pol' transmissions, $T^{0^\circ}_{\rm cp}$ and $T^{0^\circ}_{\rm xp}$, are the spectral responses of the HWP near one of the transmission maxima (called 0° here), between parallel and perpendicular polarizers, respectively. The inferred co-pol/cross-pol transmissions and modulation efficiency of

[7] The analytical relations apply, strictly speaking, at 80 K and for $k \lesssim 33\,{\rm cm}^{-1}$, thus we corroborate them at higher frequencies with the data points, which apply at ≲60 K. It is evident that the sapphire absorption coefficient has a very weak dependence on temperature below 80 K, and in particular data points collected at 1.5 K are in good enough agreement (within 2 per cent on the resulting absorption for $d = 2.5$ mm) with those collected at higher temperatures (up to 80 K). Therefore, we can safely claim that for our application the two analytical relations shown in Fig. 12 are a good representation of the sapphire absorption at 4 K.

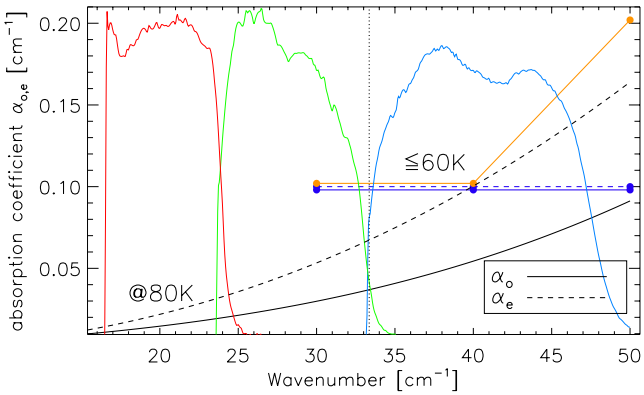

Figure 12. Ordinary (solid) and extraordinary (dashed) sapphire absorption coefficient as a function of wavenumber, at cryogenic temperatures. The two analytical relations covering the whole frequency range are derived by Savini (2010, private communication) from a set of spectral measurements of a sample at 80 K, and, strictly speaking, only apply at frequencies $\lesssim$1 THz (dotted vertical line). For reference, we plot measurements from Loewenstein et al. (1973, purple) at 1.5 K and Cook & Perkowitz (1985, ochre) at 60 K, displaced by 0.002 cm^{-1} in y for visual clarity; the lines connecting these data points follow the convention shown in the legend.

the BLASTPol HWP (with its axis at 0°) at 4 K are shown in Fig. 13. For a flat-spectrum input source, the band-integrated transmission of the HWP at its maxima is ∼0.87, ∼0.91 and ∼0.95 at 250, 350 and 500 μm, respectively; whereas the band-integrated cross-pol is $\lesssim$0.5 per cent, $\lesssim$0.2 per cent and $\lesssim$0.5 per cent, respectively; finally, the band-integrated modulation efficiency is ∼98.8, ∼99.5 and ∼99.0 per cent, respectively.

4 EMPIRICAL MODELLING

The final goal of this section is to provide a set of usable parameters that completely describe the performance of the HWP as measured in the laboratory. This set of parameters consists of the 16 coefficients of the Mueller matrix of a generic HWP, and the actual phase shift. For an ideal HWP, the Mueller matrix at $\theta = 0°$ reads (Collett 1993)

$$\mathbf{M}_{\rm HWP} = \begin{pmatrix} 1 & 0 & 0 & 0 \\ 0 & 1 & 0 & 0 \\ 0 & 0 & -1 & 0 \\ 0 & 0 & 0 & -1 \end{pmatrix}, \tag{3}$$

and the phase shift is $\Delta\varphi = 180°$.

For a real HWP, these parameters always depart from the ideal case to some extent, and certainly depend upon frequency. In the following, we describe an empirical model that we develop specifically for the characterization of the BLASTPol HWP, though we note that it can be applied to any HWP to recover its frequency-dependent descriptive parameters. Such an empirical model is complementary to the physical and analytical one developed by Savini et al. (2006, 2009), which produces an analogous output by modelling the non-idealities of the components of the HWP assembly and their optical parameters.

4.1 Mueller matrix characterization

By recalling the Stokes formalism, we can formalize the experimental apparatus described in Section 3.1 as a series of matrix products,

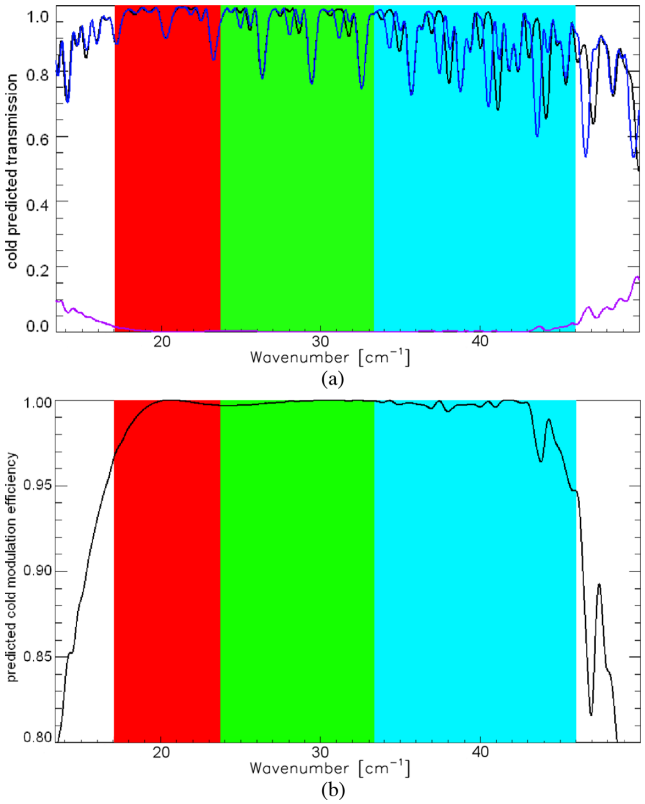

Figure 13. Derived performance of the BLASTPol HWP at 4 K, extrapolated from a set of spectral data collected with the HWP cooled to ∼120 K (see Section 3.2). 'Co-pol' and 'cross-pol' transmissions, $T_{\rm cp}$ and $T_{\rm xp}$, are defined as in Fig. 2. The approximate extent of the BLASTPol bands is also indicated. (a) The derived transmissions through the cold HWP as a function of wavenumber. The black line shows the HWP transmission, $T_{\rm cp}^{0°}$, between two parallel polarizers ($Q = 1 \rightarrow Q = 1$) with the HWP near one maximum (0°). The dark blue line shows $Q = -1 \rightarrow Q = -1$ in the same reference frame (or equivalently $Q = 1 \rightarrow Q = 1$ with the HWP axis at 90°). The purple line shows the transmission, $T_{\rm xp}^{0°}$, with the HWP axis at 0° between two perpendicular polarizers. (b) Derived modulation efficiency of the cold HWP as a function of wavenumber, obtained as $(T_{\rm cp}^{0°} - T_{\rm xp}^{0°})/(T_{\rm cp}^{0°} + T_{\rm xp}^{0°})$. Note that the y-axis scale ranges from 0.8 to 1.

as follows:

$$S_{\rm out}^{\rm cp} = \boldsymbol{D}^{\rm T} \cdot \mathbf{M}_{\rm p}^{\rm h} \cdot \mathbf{R}(-\theta) \cdot \mathbf{M}_{\rm HWP} \cdot \mathbf{R}(\theta) \cdot \boldsymbol{S}_{\rm in}^{\rm h}; \tag{4}$$

$$S_{\rm out}^{\rm xp} = \boldsymbol{D}^{\rm T} \cdot \mathbf{M}_{\rm p}^{\rm v} \cdot \mathbf{R}(-\theta) \cdot \mathbf{M}_{\rm HWP} \cdot \mathbf{R}(\theta) \cdot \boldsymbol{S}_{\rm in}^{\rm h}. \tag{5}$$

Here $\boldsymbol{D}$ is the Stokes vector for a bolometric (polarization insensitive) intensity detector, $\mathbf{M}_{\rm p}^{\rm h}$ is the Mueller matrix of an ideal horizontal polarizer, $\mathbf{M}_{\rm p}^{\rm v}$ is that of an ideal vertical polarizer, $\mathbf{R}(\theta)$ is the generic Mueller rotation matrix and $\boldsymbol{S}_{\rm in}$ is the horizontally polarized input beam from the pFTS. By expanding all the matrices in equation (4),

$$S_{\rm out}^{\rm cp} = \begin{pmatrix} 1 & 0 & 0 & 0 \end{pmatrix} \cdot \begin{pmatrix} 1 & 1 & 0 & 0 \\ 1 & 1 & 0 & 0 \\ 0 & 0 & 0 & 0 \\ 0 & 0 & 0 & 0 \end{pmatrix}$$

$$\cdot \begin{pmatrix} 1 & 0 & 0 & 0 \\ 0 & \cos(2\theta) & \sin(2\theta) & 0 \\ 0 & -\sin(2\theta) & \cos(2\theta) & 0 \\ 0 & 0 & 0 & 1 \end{pmatrix} \cdot \begin{pmatrix} a_{00} & a_{01} & a_{02} & a_{03} \\ a_{10} & a_{11} & a_{12} & a_{13} \\ a_{20} & a_{21} & a_{22} & a_{23} \\ a_{30} & a_{31} & a_{32} & a_{33} \end{pmatrix}$$

$$\cdot \begin{pmatrix} 1 & 0 & 0 & 0 \\ 0 & \cos(2\theta) & -\sin(2\theta) & 0 \\ 0 & \sin(2\theta) & \cos(2\theta) & 0 \\ 0 & 0 & 0 & 1 \end{pmatrix} \cdot \begin{pmatrix} 1 \\ 1 \\ 0 \\ 0 \end{pmatrix}, \tag{6}$$

we can compute the products and rearrange as

$$S_{\rm out}^{\rm cp} = \frac{1}{2}[2a_{00} + a_{11} + a_{22} + 2(a_{01} + a_{10})\cos 2\theta + (a_{11} - a_{22}) \times \cos 4\theta - 2(a_{02} + a_{20})\sin 2\theta - (a_{12} + a_{21})\sin 4\theta] \tag{7}$$

$$= A + B\sin 2\theta + C\cos 2\theta + D\sin 4\theta + E\cos 4\theta, \tag{8}$$

with

$$A \equiv a_{00} + \frac{a_{11}}{2} + \frac{a_{22}}{2},$$

$$B \equiv -(a_{02} + a_{20}), \quad C \equiv a_{01} + a_{10},$$

$$D \equiv -\frac{1}{2}(a_{12} + a_{21}), \quad E \equiv \frac{1}{2}(a_{11} - a_{22}). \tag{9}$$

Similarly, noting that

$$\mathbf{M}_{\rm p}^{\rm v} = \begin{pmatrix} 1 & -1 & 0 & 0 \\ -1 & 1 & 0 & 0 \\ 0 & 0 & 0 & 0 \\ 0 & 0 & 0 & 0 \end{pmatrix},$$

we rearrange equation (5) as

$$S_{\rm out}^{\rm xp} = A' + B'\sin 2\theta + C'\cos 2\theta + D'\sin 4\theta + E'\cos 4\theta, \tag{10}$$

with

$$A' \equiv a_{00} - \frac{a_{11}}{2} - \frac{a_{22}}{2},$$

$$B' \equiv a_{20} - a_{02}, \quad C' \equiv a_{01} - a_{10},$$

$$D' \equiv \frac{1}{2}(a_{12} + a_{21}), \quad E' \equiv \frac{1}{2}(a_{22} - a_{11}). \tag{11}$$

Finally, by performing linear combinations of the quantities defined in equations (9) and (11), one can write the individual elements that compose the Mueller matrix of a generic HWP as

$$a_{00} = \frac{1}{2}\left(A + A'\right), \quad a_{01} = \frac{1}{2}\left(C + C'\right),$$

$$a_{10} = \frac{1}{2}\left(C - C'\right), \quad a_{11} = \frac{1}{2}\left(A - A' + E - E'\right),$$

$$a_{02} = -\frac{1}{2}\left(B + B'\right), \quad a_{20} = \frac{1}{2}\left(B' - B\right),$$

$$a_{22} = \frac{1}{2}\left(A - A' - E + E'\right), \quad a_{12} = a_{21} = \frac{1}{2}\left(D' - D\right), \tag{12}$$

where in the last equality, we currently assume the symmetry of two coefficients, $a_{12} = a_{21}$. This degeneracy may be broken by imposing the conservation of energy, i.e. by requiring the output Stokes vector resulting from a generic polarized input travelling through the recovered HWP Mueller matrix to satisfy $I^2 = Q^2 + U^2$. Alternatively, the degeneracy can be broken by taking spectra at an intermediate configuration between co- and cross-pol; this additional constraint will be included in a future work (Spencer et al., in preparation). Also, because our experimental setup is sensitive to linear but not circular polarization, this method only allows us to constrain the nine elements of the Mueller matrix associated with [I, Q, U]. The remaining seven coefficients associated with V can only be measured with the use of a quarter-wave plate, which induces a phase shift of 90° between the two orthogonal polarizations travelling through the plate; this measurement is beyond the scope of this paper and not pertinent to the needs of BLASTPol.

We want to estimate the nine coefficients derived in equation (12) from the co-pol and cross-pol data cubes described in Section 3.2. Equations (8) and (10) encode a simple dependence of $S_{\rm out}^{\rm cp}$ and $S_{\rm out}^{\rm xp}$ upon θ, the HWP rotation angle. Therefore, for a given frequency, a fitting routine can be applied to the measured transmission curves as a function of θ, to determine the parameter sets [A, B, C, D, E] and [A', B', C', D', E'] for the co-pol and cross-pol configurations, respectively. By repeating the fit for every frequency, we have an estimate of the nine coefficients as a function of wavelength. However, this procedure does not allow us to associate an uncertainty to our estimates.

A better approach to this problem is to use a Monte Carlo simulation. We repeat the above fitting procedure 1000 times; every time we add to every individual transmission curve a realization of white noise, scaled to the 1σ spectral uncertainty as estimated in Fig. 8, and compute the fit using this newly generated transmission curve. In addition, for every frequency we introduce a random jitter on the rotation angle that has a 1σ amplitude of 1°. The dispersion in the fitted parameters due to these two types of uncertainties, which are inherent to the measurement process, provides a realistic estimate of the uncertainty associated with each of the nine coefficients. In particular, at each frequency, we produce nine histograms of the 1000 fitted values. We use the mode of each distribution as our best estimate for the corresponding coefficient at that frequency, and the 68 per cent confidence interval as the associated 1σ error.

In Fig. 14, we show a graphical representation of the nine-element Mueller matrix of the BLASTPol HWP at a given angle ($\theta = 0°$), as a function of wavenumber. In Fig. 15, we show the resulting histograms for the nine coefficients at 20 cm^{-1}, central frequency of the 500 μm BLASTPol band; histograms at 28.57 cm^{-1} (350 μm) and 40.02 cm^{-1} (250 μm) look very similar and thus are not presented here for brevity.

4.2 Position of the HWP equivalent axes

The behaviour of the coefficients as a function of wavenumber shown in Fig. 14 confirms that the position of the HWP equivalent axes, $\beta_{\rm ea}$ hereafter, has an inherent frequency dependence, which we must investigate. $\beta_{\rm ea}$ can be readily retrieved at each frequency by locating the rotation angle that corresponds to the first minimum in the fitted transmission curve. Hence, $\beta_{\rm ea}$ is measured with respect to an arbitrary constant offset that is inherent to the specific experimental setup; we set this offset to be zero at 25 cm^{-1}. Operationally, this means that the HWP zero angle in the instrument reference frame (β_0; see equation 17) must be calibrated using the 350 μm band. A plot of $\beta_{\rm ea}$ as a function of wavenumber is given in Fig. 16.

As anticipated, it is of crucial importance to derive the band-averaged value of $\beta_{\rm ea}$ for input sources with different spectral

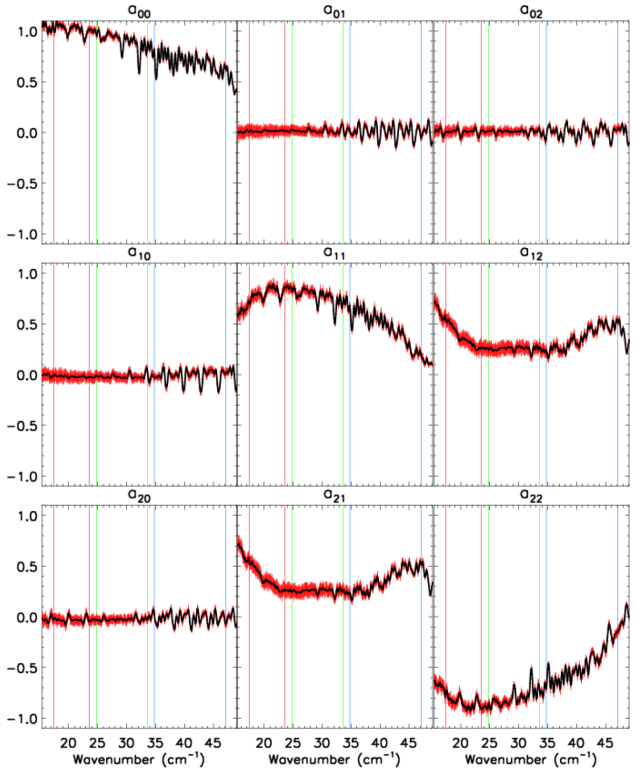

Figure 14. Graphical representation of the Mueller matrix of the BLASTPol HWP at a given angle ($\theta = 0°$), as a function of wavenumber. The (10σ) error bars (in red) are quantified via a Monte Carlo, which accounts for random errors in the spectra of amplitude as given in Fig. 8, and random errors of amplitude 1° in the rotation angle.

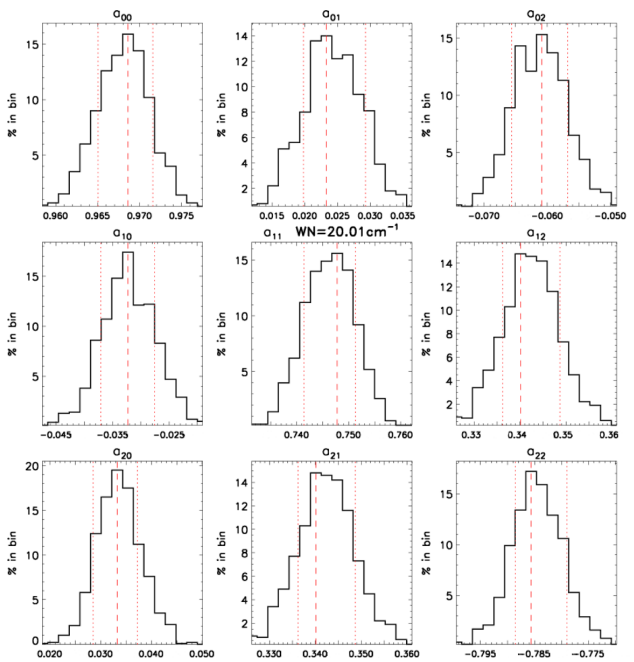

Figure 15. Histograms at $20\,\mathrm{cm}^{-1}$ (central frequency of the 500 μm BLASTPol band) resulting from the Monte Carlo fit of the HWP parameters. For every histogram, the dashed red line indicates the mode of the distribution, which we adopt as our best estimate for the corresponding coefficient at that frequency, while the two dotted red lines indicate the 68 per cent confidence interval, which we use as the uncertainty on the retrieved coefficient.

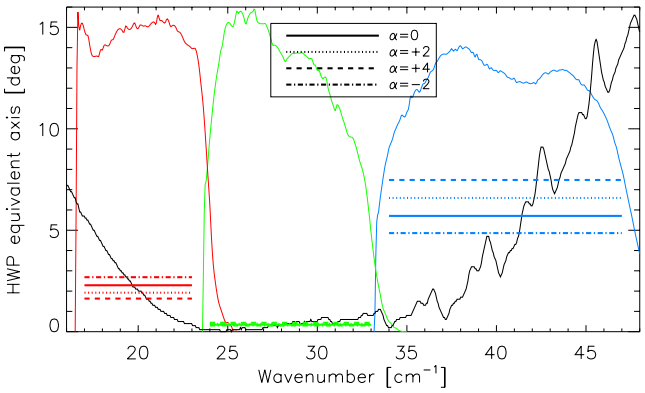

Figure 16. Position of the HWP equivalent axis, β_{ea}, as a function of wavenumber (solid black line). Note that this quantity is defined with respect to an arbitrary constant offset that is inherent to the specific experimental setup; we set this offset to be zero at $25\,\mathrm{cm}^{-1}$. The band-averaged values for input sources with different spectral index (α; see legend) are drawn as thick horizontal lines. Also shown for reference is the relative spectral response of the three BLASTPol channels, in arbitrary units.

Table 2. Band-averaged position of the HWP equivalent axis for sources with different spectral index. The input source is assumed to have a spectrum $\varsigma \propto \nu^{\alpha}$.

	$\overline{\beta}_{\mathrm{ea}}$ (°)		
α	250 μm	350 μm	500 μm
−2	4.9	0.30	2.7
0	5.7	0.35	2.3
+2	6.6	0.39	1.9
+4	7.5	0.44	1.6

signature, as follows:

$$\overline{\beta}^{\mathrm{ch}}_{\mathrm{ea}} = \frac{\int_0^{\infty} \Sigma^{\mathrm{ch}}(\nu)\, \beta_{\mathrm{ea}}(\nu)\, \varsigma(\nu)\, \mathrm{d}\nu}{\int_0^{\infty} \Sigma^{\mathrm{ch}}(\nu)\, \varsigma(\nu)\, \mathrm{d}\nu}, \tag{13}$$

where we adopt the same notation as in equation (2) and the known (or assumed) spectrum of an astronomical or calibration source is modelled as $\varsigma(\nu) \propto \nu^{\alpha}$. We compute equation (13) for a range of spectral indices of interest: $\alpha = 0$ for a flat spectrum; $\alpha = 2$ for the Rayleigh–Jeans tail of a blackbody; $\alpha = 4$ for interstellar dust, modelled as a modified blackbody with emissivity $\beta = 2$ (Hildebrand 1983); and finally $\alpha = -2$ as a replacement for the mid-infrared exponential on the Wien side of a blackbody to account for the variability of dust temperatures within a galaxy (Blain 1999; Blain, Barnard & Chapman 2003). The results of this analysis are shown in Fig. 16 and in Table 2.

As expected, the impact of different input spectral signatures is minimal at 350 μm, where the HWP has been designed to function optimally (see Section 2.2); whereas the spectral dependence is more pronounced at 250 and 500 μm, and, if neglected, it may lead to an arbitrary rotation of the retrieved polarization angle on the sky of magnitude $2\overline{\beta}_{\mathrm{ea}} = 10$–$15°$ (3–5°) at 250 (500) μm (see equation 17).

We have thus confirmed that the dependence of the HWP equivalent axes upon wavelength is inherent to the achromatic design. We now postulate that most of the non-idealities we see in the measured HWP Mueller matrix (Fig. 14) are primarily due to the wavelength dependence of β_{ea}, along with the residual absorption from

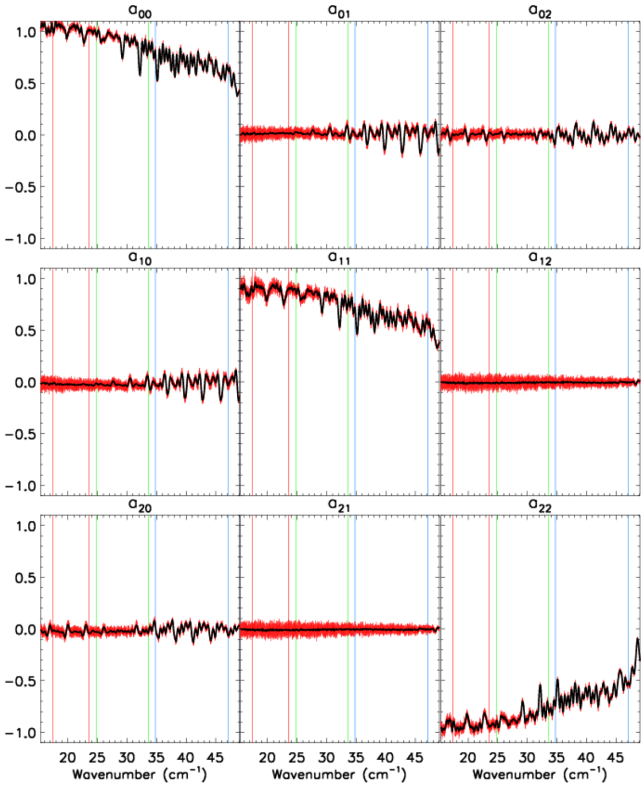

Figure 17. Graphical representation of the Mueller matrix of the BLASTPol HWP, equivalent to that shown in Fig. 14, but including in the fit the frequency-dependent position of the HWP equivalent axes (see Fig. 16).

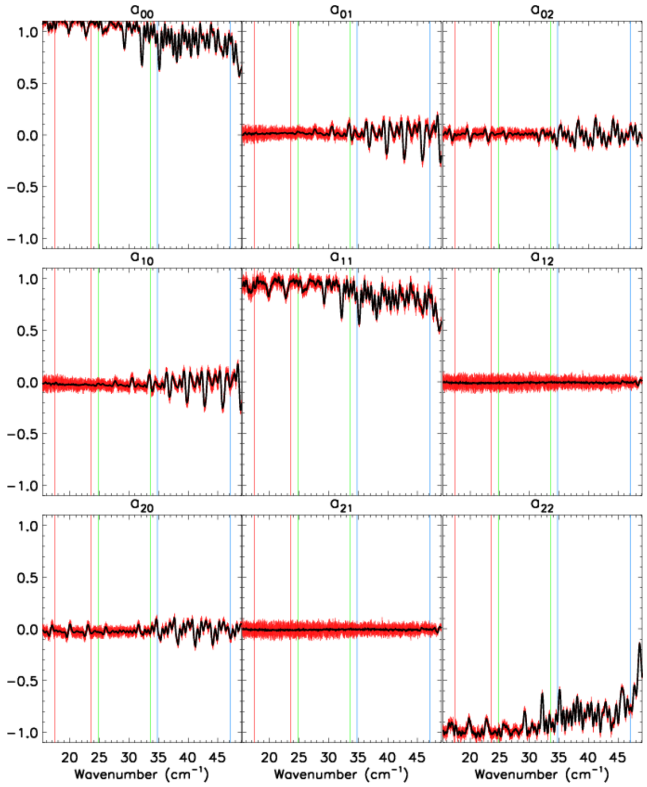

Figure 18. Graphical representation of the Mueller matrix of the BLASTPol HWP, equivalent to that shown in Fig. 17, but including a correction for the temperature dependence of the sapphire absorption coefficient (see Fig. 12).

sapphire at ∼120 K. One can imagine that the HWP performance would approach the ideal case once this effect is corrected for.

Therefore, we include $\beta_{\rm ea}(\nu)$ in our Monte Carlo as a frequency-dependent offset in the array of rotation angles (so that $\theta \rightarrow \theta - \beta_{\rm ea}$), and repeat our simulations. The results, presented in Fig. 17, can now be qualitatively compared to the Mueller matrix of an ideal HWP (equation 3). The improvement is noticeable, especially in the off-diagonal elements, and the resemblance to an ideal HWP is remarkable across the entire spectral range of interest; this procedure effectively acts to diagonalize the HWP Mueller matrix. However, the transmission losses due to absorption from the sapphire at ∼120 K still affect the diagonal elements of the matrix, as expected.

As a final improvement, we extrapolate the $\beta_{\rm ea}$-corrected HWP Mueller matrix to 4 K by including in our Monte Carlo a correction for the residual sapphire absorption (using the data presented in Fig. 12). The results are shown in Fig. 18. Although there still seems to be residual transmission losses due to sapphire absorption at 250 and 350 μm, the retrieved HWP Mueller matrix is nearly that of an ideal HWP. The band-averaged values of the matrix coefficients for a flat-spectrum input source are reported in Table 3, along with their propagated uncertainty; the off-diagonal elements are always consistent with zero within 2σ and the modulus of the three diagonal coefficients is always >0.8. The combination of these coefficients with the band-averaged values of $\beta_{\rm ea}$ given in Table 2 gives a complete account of the HWP non-idealities to the best of our ability.

We repeat the calculation of the band-averaged coefficients for the other spectral indices discussed in Fig. 16; we find values that

Table 3. Band-averaged Mueller matrix coefficients. These values are relative to Fig. 18. The input source is assumed to have a flat spectrum in frequency.

Band	250 μm	350 μm	500 μm
$\overline{a}_{00}$	0.905 ± 0.006	1.001 ± 0.006	1.008 ± 0.007
$\overline{a}_{01}$	0.012 ± 0.010	0.017 ± 0.010	0.014 ± 0.011
$\overline{a}_{02}$	−0.002 ± 0.008	0.006 ± 0.009	0.001 ± 0.009
$\overline{a}_{10}$	−0.016 ± 0.010	−0.021 ± 0.010	−0.020 ± 0.011
$\overline{a}_{11}$	0.806 ± 0.011	0.928 ± 0.010	0.935 ± 0.012
$\overline{a}_{12}$	−0.007 ± 0.011	−0.009 ± 0.014	−0.011 ± 0.014
$\overline{a}_{20}$	−0.008 ± 0.008	−0.022 ± 0.010	−0.021 ± 0.010
$\overline{a}_{21}$	−0.007 ± 0.011	−0.009 ± 0.014	−0.011 ± 0.014
$\overline{a}_{22}$	−0.808 ± 0.008	−0.960 ± 0.009	−0.979 ± 0.010

are always within 1–2 per cent of those reported in Table 3, and thus we do not explicitly report them here. Because the three diagonal elements of the HWP Mueller matrix effectively determine the HWP co-pol/cross-pol transmission and modulation efficiency, this analysis confirms that these quantities are very weakly dependent on the spectral index of the input source; these findings are in very good agreement with those of Savini et al. (2009). We will see in Section 5 how $\overline{a}_{00}$, $\overline{a}_{11}$ and $\overline{a}_{22}$ can be incorporated in the map-making algorithm in terms of optical efficiency, η, and polarization efficiency, ε, of each detector.

4.3 Effective HWP phase shift

Finally, we discuss a potential limitation to any linear polarization modulator, i.e. the leakage between axes. In an HWP, the phase

shift between the two axes should be as close to 180° as possible to avoid transforming linear into elliptical polarization, hence losing modulation efficiency. The phase cannot be directly measured in a pFTS, but it can be indirectly inferred from the HWP Mueller matrix.

In order to recover the wavelength-dependent phase shift of the HWP, we recall the Mueller matrix of a non-ideal impedance-matched single birefringent slab (Savini et al. 2009, at $\theta = 0°$):

$$\mathbf{M}_{\rm slab}(\theta = 0°, \Delta\varphi) = \frac{1}{2} \times \begin{pmatrix} \tau_\parallel^2 + \tau_\perp^2 & \tau_\parallel^2 - \tau_\perp^2 & 0 & 0 \\ \tau_\parallel^2 - \tau_\perp^2 & \tau_\parallel^2 + \tau_\perp^2 & 0 & 0 \\ 0 & 0 & 2\,\tau_\parallel\,\tau_\perp \cos\Delta\varphi & 2\,\tau_\parallel\,\tau_\perp \sin\Delta\varphi \\ 0 & 0 & -2\,\tau_\parallel\,\tau_\perp \sin\Delta\varphi & 2\,\tau_\parallel\,\tau_\perp \cos\Delta\varphi \end{pmatrix}, \tag{14}$$

where $\tau_\parallel^2$ and $\tau_\perp^2$ are the measured transmissions of orthogonal polarizations aligned with the birefringent axes. By comparing the matrix in equation (14) with that of a generic HWP, we can solve for the HWP phase shift as

$$\cos\Delta\varphi = \frac{a_{22}}{2}\left(\frac{a_{00}+a_{01}}{2}\right)^{-\frac{1}{2}}\left(\frac{a_{00}-a_{01}}{2}\right)^{-\frac{1}{2}}. \tag{15}$$

Equation (15) allows us to recover the phase shift from our knowledge of a_{00}, a_{01} and a_{22}. Fig. 19 shows the estimated phase shift of the BLASTPol HWP as a function of wavenumber, after the introduction in our Monte Carlo routine of the wavelength-dependent position of the HWP equivalent axes depicted in Fig. 16.

Clearly, the $\beta_{\rm ea}$-corrected phase shift (in black) appreciably departs from 180°. However, recall that equation (15) strictly applies only to a single birefringent plate. In a multislab Pancharatnam stack, $\Delta\varphi$ becomes an 'effective' phase shift as we are no longer in the presence of a pure cosine modulation, thus slightly skewing the HWP modulation function and resulting in an artificially higher leakage between axes when the cosine function is inverted.

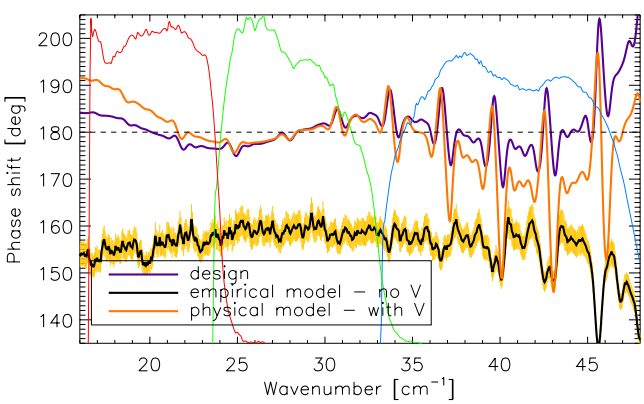

Figure 19. Phase shift of the BLASTPol HWP as a function of wavenumber. The purple line shows the design goal and the orange line shows the *as-built* phase shift, estimated using the physical model of Savini et al. (2006, see Section 3.4), which accounts for the depolarization effects due to standing waves between sapphire substrates by estimating the circular polarization (V) portion of the HWP Mueller matrix. On the other hand, our empirical model (in black, with 3σ error bars in yellow) underestimates the phase shift because (in the absence of the V terms) we have assumed a pure cosine modulation, which is not adequate in a multi-slab Pancharatnam stack. Also shown for reference are the ideal phase shift for an HWP (180°) and the relative spectral response of the three BLASTPol channels, in arbitrary units.

Our empirical method, which does not estimate the circular polarization (V) portion of the HWP Mueller matrix, is prone to underestimating the phase shift by mistaking the depolarization effects due to standing waves between sapphire substrates (enhanced by the presence of the interspersed polyethylene layers) for a phase deficit. In fact, were the phase shift really $\lesssim$160°, we would get a substantially higher cross-pol on the FTS measurements than the $\lesssim$0.5 per cent we measure in Figs 5 and 13(a).

While none of the other quantities estimated in the previous sections are affected by this deficiency in our model, we redress for the inadequacy of our empirical model in retrieving the phase shift by resorting to the physical model of Savini et al. (2006, discussed in Section 3.4). The purple line in Fig. 19 shows the design goal for the BLASTPol HWP, which is computed by assuming the nominal values for the HWP build parameters (see Table 1), while the orange line shows the as-built phase shift, which is obtained by fitting the spectral data and allowing the build parameters to vary in a physical way around the nominal values.

The physical model is able to reconstruct the inevitable substrate alignment errors that occur during the HWP assembly and provides a much improved estimate of the actual phase shift, which is within ∼5° of the ideal value for the central BLASTPol band (350 μm, where the HWP is optimized). Although the side bands show worse performance (within ∼15° of 180°), we have indications that the modulation efficiency of the HWP at 4 K is only mildly affected by this departure from ideality. From Fig. 13(b), we see that the extrapolated HWP modulation efficiency is always above 95 per cent across the whole spectral range of interest, with band-integrated values exceeding 98 per cent. Moreover, phase shift deviations of similar amplitude are measured in most (sub)mm-wave achromatic HWPs manufactured to date (e.g. Savini et al. 2009; Zhang et al. 2011).

In addition to the non-ideal substrate alignment, the physical model yields a best-fitting thickness for the individual sapphire substrates that is 9.6 μm smaller than the nominal value of 500 μm available in the market.[8] While it is beyond the scope of this paper to quantify exactly the relative contributions of plate misalignment and reduced thickness to the overall non-ideal behaviour of the phase shift, we cannot rule out a contribution from both effects. Furthermore, and more importantly, neither of these two effects has nearly the same impact on the other performance parameters presented in the previous sections (the nine Mueller matrix coefficients associated with linear polarization) because of their weak dependence on the phase shift.

Incidentally, we verify that our methodology does not violate conservation of energy by ensuring that the output Stokes vector resulting from a generic polarized input travelling through the recovered HWP Mueller matrix satisfies $I^2 \geq Q^2 + U^2$ in every instance described above.

5 MAP-MAKING ALGORITHM

Map-making is the operation that generates an astronomical map, which contains in every pixel an estimate of the sky emission, and is obtained by combining data from all detectors available at a

[8] We verify that the sum of the thicknesses from Table 1 is compatible with the overall measured thickness of the HWP stack.

given wavelength channel, their noise properties and the pointing information. The raw BLAST(Pol) data consist of bolometer time-ordered streams, which are cleaned and pre-processed before being fed into the map-maker; the details are extensively described elsewhere (Rex 2007; Truch 2007; Pascale et al. 2008; Wiebe 2008), and we refer to these works for a complete account of the low-level data reduction.

In the following, we focus on the mathematical formalism of the map-making technique, and its algorithmic implementation in the specific case of BLASTPol.

For a non-ideal polarization experiment, by adopting the Stokes formalism and assuming that no circular (V) polarization is present, we can model the data as

$$d_t^i = \frac{\eta^i}{2} A_{tp}^i \left[I_p + \varepsilon^i \left(Q_p \cos 2\gamma_t^i + U_p \sin 2\gamma_t^i \right) \right] + n_t^i. \tag{16}$$

Here i, t and p label detector index, time and map pixel, respectively; d_t^i are the time-ordered data for a given channel, related to the sky maps $[I_p, Q_p, U_p]$ by the pointing operator A_{tp}^i; η^i is the optical efficiency of each detector; ε^i is the polarization efficiency of each detector with its polarizing grid (analyser); and n_t^i represents a generic time-dependent noise term. Throughout this discussion, it is assumed that the term within square brackets is the convolution of the sky emission with the telescope point spread function. γ_t^i is the time-ordered vector of the observed polarization angle, defined as the angle between the polarization reference vector at the sky pixel p (in the chosen celestial frame) and the polarimeter transmission axis. γ_t^i is given by

$$\gamma_t^i = \alpha_t^i + 2 \left[\beta_t - \beta_0 - \overline{\beta}_{\rm ea} \right] + \delta_{\rm grid}^i, \tag{17}$$

where α_t^i is the angle between the reference vector at pixel p and a vector pointing from p to the zenith along a great circle, β_t is the HWP orientation angle in the instrument frame, β_0 is the HWP zero angle in the instrument frame, $\overline{\beta}_{\rm ea}$ is the band-averaged position of the equivalent axes of the HWP (dependent on the known or assumed spectral signature of the input source; see Section 4.2), and $\delta_{\rm grid}^i = [0, \pi/2]$ accounts for the transmission axis of the polarizing grids being parallel/perpendicular to the zenith angle.

The notation outlined above can be connected to the Mueller formalism developed in Section 4.1 to determine under which circumstances equation (16) is valid in the presence of a real (i.e. non-ideal) HWP. Because we have included in equation (17) the band-averaged position of the equivalent axes of the HWP, $\overline{\beta}_{\rm ea}$, the Mueller matrix of the BLASTPol HWP can be considered almost that of an ideal HWP, as discussed in Section 4.2. Nonetheless, we have shown that the band-averaged values of the three diagonal matrix coefficients are not identically unity (but always >0.8 in modulus), probably as a result of residual absorption from sapphire, especially in the 250 and 350 μm bands (although we have corrected for it to the best of our knowledge).

In the light of these considerations, we now want to compare equation (16) to equation (8), which both represent the signal measured by a polarization insensitive intensity detector when illuminated by a polarized input that propagates through a rotating HWP and an analyser. A term-by-term comparison shows that these two expressions are equivalent when the coefficients B and C (defined in equation 9) are zero, i.e. when the HWP modulates the polarization purely at four times the rotation angle, with no leakage in the second harmonic (twice the rotation angle) and thus no leakage of I into Q and U. These two coefficients are linear combinations of the HWP Mueller matrix elements $\overline{a}_{01}, \overline{a}_{10}, \overline{a}_{02}, \overline{a}_{20}$, which we have shown in Table 3 to be all compatible with zero within 2σ. In addition, their amplitude is at most ∼2 per cent of that of the diagonal matrix elements, so to first order the coefficients B and C can be neglected, and the two expressions can be considered equivalent. Nonetheless, these generally moderate levels of $I \rightarrow Q, U$ leakage can be readily accounted for by incorporating in the map-making algorithm a correction for the 'instrumental polarization' (IP; see Matthews et al. 2013; Angilè et al., in preparation).

In addition, after some simple algebra, it can be shown that $\eta = a_{00} + \frac{a_{11}}{2} + \frac{a_{22}}{2}$ and $\eta\,\varepsilon = \frac{a_{11}}{2} - \frac{a_{22}}{2}$. As anticipated in Section 4.2, the knowledge of the band-averaged values of the three diagonal matrix elements, $\overline{a}_{00}, \overline{a}_{11}, \overline{a}_{22}$ (which we have shown to depend weakly on the spectral index of the input source), can be readily incorporated in the map-making algorithm in terms of optical efficiency, η, and polarization efficiency, ε, of the HWP; these can be factored into the overall optical and polarization efficiency of each detector, which are the product of several factors (e.g. bolometer absorption efficiency, HWP efficiency, absorption in the optical chain, etc.). From the values listed in Table 3, in our case we find $[\eta_{\rm hwp}, \varepsilon_{\rm hwp}] = [0.904, 0.893]$, $[0.985, 0.958]$ and $[0.986, 0.971]$ at 250, 350 and 500 μm, respectively.

Finally, the comparison of equations (16) and (8) also yields the relation $\eta\,\varepsilon\,\chi = -a_{12} = -a_{21}$, where we have introduced a new parameter, χ, which quantifies the amplitude of the mixing of Q and U. From Table 3, we see that $\overline{a}_{12} = \overline{a}_{21}$ are always compatible with zero within 1σ, and their amplitude is at most ∼1 per cent of that of the diagonal matrix elements. Nonetheless we quantify the amplitude of the $Q \leftrightarrow U$ mixing to be $\chi_{\rm hwp} = 0.009$, 0.010 and 0.011 at 250, 350 and 500 μm, respectively. While this correction is not currently included in our algorithm, we indicate that it can be implemented in a relatively straightforward way by modifying equation (16) with a double change of variable, i.e. $Q \rightarrow Q + \chi U$ and $U \rightarrow U + \chi Q$. If χ is estimated to the required accuracy, the unmixed Q and U can be retrieved unbiasedly. This correction may be very relevant to CMB polarization experiments, where any $Q \leftrightarrow U$ leakage leads to a spurious mixing of the EE and BB modes.

We remind the reader that the above factors have been computed directly from the band-averaged coefficients of the inferred HWP Mueller matrix extrapolated to 4 K, and offer a direct way to include the modelled HWP non-idealities in a map-making algorithm. On the other hand, the band-averaged HWP maximum transmission, polarization efficiency and cross-pol quoted at the end of Section 3 are estimated directly from the spectra extrapolated to 4 K, and are mostly informative from an experimental point of view rather than for data analysis purposes.

Consider now one map pixel p that is observed in one band by k detectors ($i = 1, \ldots, k$); let us define the generalized pointing matrix $\mathbf{A}_{tp}$, which includes the trigonometric functions along with the efficiencies,

$$\mathbf{A}_{tp} \equiv \frac{1}{2} \begin{pmatrix} \eta^1 A_{tp}^1 & \eta^1 \varepsilon^1 A_{tp}^1 \cos 2\gamma_t^1 & \eta^1 \varepsilon^1 A_{tp}^1 \sin 2\gamma_t^1 \\ \vdots & \vdots & \vdots \\ \eta^i A_{tp}^i & \eta^i \varepsilon^i A_{tp}^i \cos 2\gamma_t^i & \eta^i \varepsilon^i A_{tp}^i \sin 2\gamma_t^i \\ \vdots & \vdots & \vdots \\ \eta^k A_{tp}^k & \eta^k \varepsilon^k A_{tp}^k \cos 2\gamma_t^k & \eta^k \varepsilon^k A_{tp}^k \sin 2\gamma_t^k \end{pmatrix}, \tag{18}$$

and the map triplet $\mathbf{S}_p$, along with the combined detector ($\boldsymbol{D}_t$) and noise ($\boldsymbol{n}_t$) timelines,

$$\mathbf{S}_p \equiv \begin{pmatrix} I_p \\ Q_p \\ U_p \end{pmatrix}, \quad \boldsymbol{D}_t \equiv \begin{pmatrix} d_t^1 \\ \vdots \\ d_t^i \\ \vdots \\ d_t^k \end{pmatrix}, \quad \boldsymbol{n}_t \equiv \begin{pmatrix} n_t^1 \\ \vdots \\ n_t^i \\ \vdots \\ n_t^k \end{pmatrix}. \tag{19}$$

Equation (16) can then be rewritten in compact form as

$$\boldsymbol{D}_t = \mathbf{A}_{tp}\, \mathbf{S}_p + \boldsymbol{n}_t. \tag{20}$$

Under the assumption that the noise is Gaussian and stationary, the likelihood of $\mathbf{S}_p$ given the data can be maximized, thus yielding the well-known generalized least squares estimator for $\mathbf{S}_p$:

$$\tilde{\mathbf{S}}_p = \left(\mathbf{A}_{tp}^{\mathrm{T}}\, \mathbf{N}^{-1}\, \mathbf{A}_{tp}\right)^{-1} \mathbf{A}_{tp}^{\mathrm{T}}\, \mathbf{N}^{-1}\, \boldsymbol{D}_t, \tag{21}$$

where $\mathbf{N} \equiv \langle \boldsymbol{n}_t\, \boldsymbol{n}_{t'} \rangle$ is the noise covariance matrix of the data in the time domain, with t, t' running over the detector time samples (typically $N_\mathrm{s} \sim 10^6$–10^7).

Computation of the solution to equation (21) is far from trivial in most astronomical applications, due to $\mathbf{N}$ being a very large matrix, of size $kN_\mathrm{s} \times kN_\mathrm{s}$. Understandably, it is computationally challenging to invert this matrix, especially when there are correlations among detectors, and a number of 'optimal' map-making techniques have been developed in the literature to tackle this problem (e.g. Natoli et al. 2001, 2009; Masi et al. 2006; Johnson et al. 2007; Wu et al. 2007; Patanchon et al. 2008; Cantalupo et al. 2010).

5.1 Naive binning

In the simple case that the noise is uncorrelated between different detectors, the matrix $\mathbf{N}$ reduces to block diagonal:

$$\langle n_t^i\, n_{t'}^j \rangle = \langle n_t^j\, n_{t'}^i \rangle = 0 \quad (i \neq j). \tag{22}$$

In addition, let us assume that there is no correlation between noise of different samples acquired by the same detector, or, in other words, that the noise in each detector is white. In this case, each 'block' of the noise covariance matrix collapses into one value, which is the timeline variance for each detector. Hence, $\mathbf{N}$ becomes a $k \times k$ diagonal matrix where the diagonal elements are the sample variances of the detectors, σ_i^2, and weights can thus be defined as the inverse of those variances, $w^i \equiv 1/\sigma_i^2$.

Therefore, under the assumption that the noise is white and uncorrelated among detectors, equation (21) reduces to a simple, weighted binning ('naive' binning; see also Benoît et al. 2004; Pascale et al. 2011) of the map:

$$\mathbf{S}_p = \begin{pmatrix} I_p \\ Q_p \\ U_p \end{pmatrix} = \frac{\sum_{i=1}^{k} \sum_{t=1}^{N_\mathrm{s}} w^i \frac{(\mathbf{A}_{tp}^i)^{\mathrm{T}}\, d_t^i}{(\mathbf{A}_{tp}^i)^{\mathrm{T}}\, \mathbf{A}_{tp}^i}}{\sum_{i=1}^{k} w^i}. \tag{23}$$

In the light of these considerations, let us go back to equation (16) and model the generic time-dependent noise term as $n_t^i = u_t + \xi^i \rho_t$, where u_t represents a time-dependent noise term, completely uncorrelated among different detectors, while ρ_t describes the correlated noise (varying over time-scales larger than the ratio of the size of the detector array to the scan speed), coupled to each detector via the ξ^i parameter, peculiar to each bolometer.

Let us define the following quantity for every pixel p in the map:

$$\mathbf{S}_p^\mathrm{e} = \begin{pmatrix} I_p^\mathrm{e} \\ Q_p^\mathrm{e} \\ U_p^\mathrm{e} \end{pmatrix} \equiv \begin{pmatrix} \sum_{i=1}^{k} \sum_{t=1}^{N_\mathrm{s}} d_t^i \\ \sum_{i=1}^{k} \sum_{t=1}^{N_\mathrm{s}} d_t^i \cos 2\gamma_t^i \\ \sum_{i=1}^{k} \sum_{t=1}^{N_\mathrm{s}} d_t^i \sin 2\gamma_t^i \end{pmatrix}, \tag{24}$$

where N_s is now the number of samples in each detector timeline that fall within pixel p, and the superscript 'e' stands for 'estimated'. The above quantities can be computed directly from the detector timelines. Recalling equation (16), we can outline the following linear system of three equations with three unknowns:

$$\begin{pmatrix} I_p^\mathrm{e} \\ Q_p^\mathrm{e} \\ U_p^\mathrm{e} \end{pmatrix} = \begin{pmatrix} \sum_{i,t} 1 & \sum_{i,t} \cos 2\gamma_t^i & \sum_{i,t} \sin 2\gamma_t^i \\ \sum_{i,t} \cos 2\gamma_t^i & \sum_{i,t} \cos^2 2\gamma_t^i & \sum_{i,t} \cos 2\gamma_t^i \sin 2\gamma_t^i \\ \sum_{i,t} \sin 2\gamma_t^i & \sum_{i,t} \cos 2\gamma_t^i \sin 2\gamma_t^i & \sum_{i,t} \sin^2 2\gamma_t^i \end{pmatrix} \cdot \frac{1}{2} \begin{pmatrix} I_p \\ Q_p \\ U_p \end{pmatrix} + \begin{pmatrix} \sum_{i,t} (u_t + \xi^i \rho_t) \\ \sum_{i,t} (u_t + \xi^i \rho_t) \cos 2\gamma_t^i \\ \sum_{i,t} (u_t + \xi^i \rho_t) \sin 2\gamma_t^i \end{pmatrix}, \tag{25}$$

where we have temporarily assumed $\eta^i = \varepsilon^i = w^i = 1$ and combined the two sums in one, with the indices i and t running, respectively, over the bolometers and the samples in each detector timeline.

If we now define the quantities,

$$N_\mathrm{hit} \equiv \sum_{i,t} \frac{1}{2}, \qquad c \equiv \sum_{i,t} \frac{1}{2} \cos 2\gamma_t^i,$$

$$c_2 \equiv \sum_{i,t} \frac{1}{2} \cos^2 2\gamma_t^i, \qquad s \equiv \sum_{i,t} \frac{1}{2} \sin 2\gamma_t^i,$$

$$s_2 \equiv \sum_{i,t} \frac{1}{2} \sin^2 2\gamma_t^i = N_\mathrm{hit} - c_2, \qquad U \equiv \sum_{i,t} u_t,$$

$$m \equiv \sum_{i,t} \frac{1}{2} \cos 2\gamma_t^i \sin 2\gamma_t^i, \qquad C_2^u \equiv \sum_{i,t} u_t \cos 2\gamma_t^i$$

$$S_2^u \equiv \sum_{i,t} u_t \sin 2\gamma_t^i, \qquad P \equiv \sum_{i,t} \xi^i \rho_t,$$

$$C_2^\rho \equiv \sum_{i,t} \xi^i \rho_t \cos 2\gamma_t^i, \qquad S_2^\rho \equiv \sum_{i,t} \xi^i \rho_t \sin 2\gamma_t^i, \tag{26}$$

then the system in equation (25) can be rewritten in compact form as

$$\begin{pmatrix} I_p^{\rm e} \\ Q_p^{\rm e} \\ U_p^{\rm e} \end{pmatrix} = \begin{pmatrix} N_{\rm hit} & c & s \\ c & c_2 & m \\ s & m & N_{\rm hit} - c_2 \end{pmatrix} \cdot \begin{pmatrix} I_p \\ Q_p \\ U_p \end{pmatrix} + \begin{pmatrix} U + P \\ C_2^u + C_2^\rho \\ S_2^u + S_2^\rho \end{pmatrix}. \tag{27}$$

In order to retrieve an estimate of $\mathbf{S}_p$ from the quantities computed in equation (24), the above system has to be solved for every pixel p in the map. One can already see the computational advantage of inverting a 3×3 matrix $N_{\rm pix} \times N_{\rm pix}$ times, with respect the inversion of a generic $kN_{\rm s} \times kN_{\rm s}$ matrix (for detectors having uncorrelated $1/f$ noise as well as a common-mode $1/f$ noise; Patanchon et al. 2008), or k matrices of size $N_{\rm s} \times N_{\rm s}$ (for detectors having only uncorrelated $1/f$ noise; Cantalupo et al. 2010). The main difficulties are, of course, in estimating the noise terms U, P, C_2^u, C_2^ρ, S_2^u, S_2^ρ. However, recalling equation (17) and the fact that adjacent detectors have orthogonal polarizing grids ($\delta^i_{\rm grid} = [0, \pi/2]$), we note that, in the sum over i, adjacent detectors have equal and opposite contributions to C_2^ρ and S_2^ρ, under the following assumptions: (i) the time-scale over which the correlated noise is approximately constant is larger than the time elapsed while scanning the same patch of sky with two adjacent detectors and (ii) ξ^i is not too dissimilar between adjacent bolometers.

This means that the terms C_2^ρ and S_2^ρ can be neglected, under the above assumptions, while estimating the $[Q, U]$ maps. In particular, as a first step, we can solve for I only by high-pass filtering the timelines, in order to suppress the correlated noise term in I, P. Subsequently, I can be assumed known, and the $[Q, U]$ maps can be computed without filtering the timelines, so that polarized signal at large angular scales is not suppressed.

The other assumption required for the naive binning is that the noise is white, at least on the time-scales relevant to BLASTPol's scan strategy. An analysis of the bolometer timelines from the 2010 campaign shows that the knee of the $1/f$ noise in the difference between two adjacent detectors is typically located at frequencies $\lesssim$0.1 Hz; assuming a typical scan speed of $0\overset{\circ}{.}1\,{\rm s}^{-1}$, this corresponds to angular scales of $\gtrsim 1^\circ$ on the sky. The regions mapped by BLASTPol hardly exceed 1° in size (see table 1.1 in Moncelsi 2011; Angilè et al. in preparation), hence here we stipulate that the noise in the difference between pairs of adjacent detectors is white.

Therefore, under the assumptions above, we can solve the linear system outlined in equation (27); by defining the following quantities,

$$\begin{aligned} &\Delta \equiv c^2\,(c_2 - N_{\rm h}) - N_{\rm h}\left(c_2^2 + m^2 - c_2\,N_{\rm h}\right) + 2\,c\,s\,m - c_2\,s^2, \\ &A \equiv -\left(c_2^2 + m^2 - c_2\,N_{\rm h}\right), \quad B \equiv c\,(c_2 - N_{\rm h}) + s\,m, \\ &C \equiv c\,m - s\,c_2, \quad D \equiv -\left[(c_2 - N_{\rm h})\,N_{\rm h} + s^2\right], \\ &E \equiv c\,s - m\,N_{\rm h}, \quad F \equiv c_2\,N_{\rm h} - c^2, \end{aligned} \tag{28}$$

the solution to the system can be written in compact form:

$$\mathbf{S}_p = \begin{pmatrix} I_p \\ Q_p \\ U_p \end{pmatrix} = \begin{pmatrix} \frac{A\,I_p^{\rm e} + B\,Q_p^{\rm e} + C\,U_p^{\rm e}}{\Delta} \\ \frac{B\,I_p^{\rm e} + D\,Q_p^{\rm e} + E\,U_p^{\rm e}}{\Delta} \\ \frac{C\,I_p^{\rm e} + E\,Q_p^{\rm e} + F\,U_p^{\rm e}}{\Delta} \end{pmatrix}, \tag{29}$$

where we have renamed $N_{\rm hit} \to N_{\rm h}$ for brevity.

5.2 Weights and uncertainties

The solution for $\mathbf{S}_p$ given in equation (29) is a simple, unweighted binning of the data into the map pixels. In reality, as anticipated in equation (23), we want to perform a weighted binning, where the weight of each detector is given by the inverse of its timeline variance, which can be easily measured as the bolometer's white noise floor level. In our formalism, the weighted binning is simply achieved by defining $[I_p^{\rm e}, Q_p^{\rm e}, U_p^{\rm e}]$ in equation (24), as well as each of the quantities $N_{\rm h}$, c, s, c_2, s_2 and m introduced in equation (26), to include w^i in the sums. Similarly, the measured values of the optical efficiencies η^i and polarization efficiencies ε^i can readily be inserted in equation (25) to account for the non-idealities of the optical system.

The introduction of the weights allows us to derive the expression for the statistical error on $\mathbf{S}_p$, in the continued assumption of uncorrelated noise, following the usual error propagation formula (e.g. Press et al. 1992, here we omit the sum over t for simplicity):

$$\sigma_p^2 = \sum_i \frac{1}{w^i} \left(\frac{\partial \mathbf{S}_p}{\partial d^i}\right)^2. \tag{30}$$

After some tedious algebra, the expression for the statistical error is

$$\sigma_p^2 = \begin{pmatrix} {\rm Var}_{\rm p}^{\rm I} \\ {\rm Var}_p^Q \\ {\rm Var}_p^U \end{pmatrix} = \begin{pmatrix} \frac{2}{\Delta^2}\left(A^2\,N_{\rm h} + B^2\,c_2 + C^2\,s_2 + 2\,A\,B\,c + 2\,A\,C\,s + 2\,B\,C\,m\right) \\ \frac{2}{\Delta^2}\left(B^2\,N_{\rm h} + D^2\,c_2 + E^2\,s_2 + 2\,B\,D\,c + 2\,B\,E\,s + 2\,D\,E\,m\right) \\ \frac{2}{\Delta^2}\left(C^2\,N_{\rm h} + E^2\,c_2 + F^2\,s_2 + 2\,C\,E\,c + 2\,C\,F\,s + 2\,E\,F\,m\right) \end{pmatrix},$$

where $s_2 \equiv N_{\rm h} - c_2$, as noted in equation (26). To first order, these expressions can be used to quantify the uncertainty of $[I, Q, U]$ in each map pixel p. A more comprehensive account of the correlations in the noise, as well as a thorough validation of the assumptions made here, is beyond the scope of this paper and will be treated in a future work.

5.3 Preliminary map

As a proof of concept of the naive binning technique for the BLASTPol polarized map-maker, which includes all the corrections due to HWP non-idealities discussed in this work, we present a *preliminary* map at 500 μm of one of the GMCs observed by BLASTPol, the Carina Nebula. In this specific case, we calculate $\overline{\beta}_{\rm ea}^{500\,\mu{\rm m}} = 1.7$ based on a dust emissivity spectral index of 1.37 (Salatino et al. 2012) for a modified blackbody spectral energy distribution.

The map in Fig. 20 is presented as contour levels of the intensity map I, on which we superimpose pseudo-vectors indicating the inferred magnetic field direction on the sky (assumed to be perpendicular to the measured polarization direction; see Lazarian 2007). The sky polarization angle is given by $\phi = \frac{1}{2}\arctan\frac{U}{Q}$. Because the absolute flux calibration has not been finalized yet, we choose not to report here the intensity values corresponding to each contour level. This map should not be considered of any scientific value as it is not calibrated in flux. Nonetheless, we find a remarkable agreement between the BLASTPol polarization directions at 500 μm and those produced by the SPARO (Novak et al. 2003) at 450 μm, which are shown in fig. 1 of Li et al. (2006) and whose pseudo-vectors are reported in Fig. 20 for comparison. Here, the original BLASTPol $[I, Q, U]$ maps have been smoothed with a kernel of 4 arcmin (full

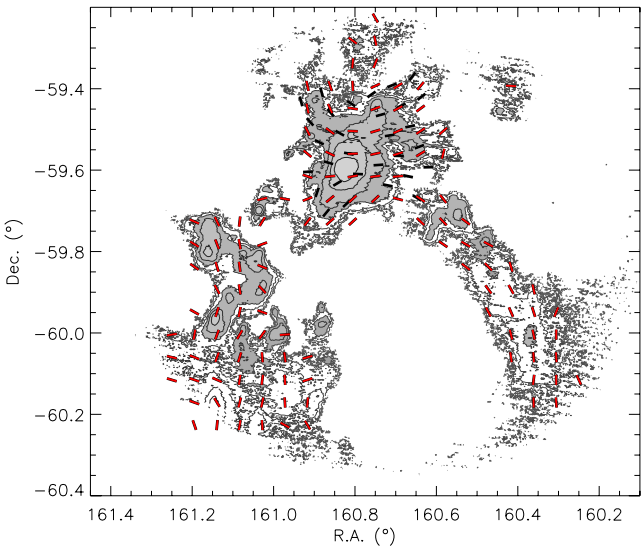

Figure 20. Preliminary BLASTPol map at 500 μm of the Carina Nebula, a GMC approximately centred at coordinates [$10^{h}42^{m}35^{s}$, $-59°42'15''$]. The intensity contour levels are shown in the background. The pseudo-vectors indicate the inferred magnetic field direction: the BLASTPol measurements (red) are in excellent agreement with those from the SPARO polarimeter at 450 μm (black; Li et al. 2006). This map should not be considered of any scientific value as no absolute calibration has been applied to the intensity contours; the map is only shown as a proof of concept for the map-maker, which includes all the corrections due to HWP non-idealities discussed in this work. Here, we adopt $\overline{\beta}_{ea}^{500\,\mu m} = 1.7$, calculated assuming a spectral index for the dust emissivity of 1.37 (Salatino et al. 2012).

width at half-maximum) for a more direct comparison with the SPARO data.

6 CONCLUDING REMARKS

The goal of the first part of this work was to identify and measure the parameters that fully characterize the spectral performance of the linear polarization modulator integrated in the BLASTPol instrument, a cryogenic achromatic HWP.

We have described in detail the design and manufacturing process of a five-slab sapphire HWP, which is, to our knowledge, the most achromatic built to date at (sub)mm wavelengths. In the same context, we have provided a useful collection of spectral data from the literature for the sapphire absorption coefficient at cryogenic temperatures.

Using a polarizing FTS, we have fully characterized the spectral response of the antireflection coated BLASTPol HWP at room temperature and at 120 K; we have acquired data cubes by measuring spectra while rotating the HWP to produce the polarization modulation.

The cold data set contains measurements in both co-pol and cross-pol configurations; we have used these two data cubes to estimate 9 out of 16 elements of the HWP Mueller matrix as a function of frequency. We have developed an ad hoc Monte Carlo algorithm that returns for every frequency the best estimate of each matrix element and the associated error, which is a combination of the uncertainty on the measured spectra and a random jitter on the rotation angle.

We have measured how the position of the equivalent axes of the HWP, β_{ea}, changes as a function of frequency, an effect that is inherent to any achromatic design. Once this dependence is accounted for in the Monte Carlo, and a correction is implemented for the residual absorption from sapphire, the Mueller matrix of the HWP approaches that of an ideal HWP, at all wavelengths of interest. In particular, the (band-averaged) off-diagonal elements are always consistent with zero within 2σ and the modulus of the three diagonal coefficients is always >0.8. Therefore, we have introduced in the BLASTPol map-making algorithm the band-integrated values of β_{ea} as an additional parameter in the evaluation of the polarization angle. To first order, this approach allows us to account for most of the non-idealities in the HWP.

We have investigated the impact of input sources with different spectral signatures on β_{ea} and on the HWP Mueller matrix coefficients. We find that the HWP transmission and modulation efficiency are very weakly dependent on the spectral index of the input source, whereas the position of the equivalent axes of the sapphire plate stack is more significantly affected. This latter dependence, if neglected, may lead to an arbitrary rotation of the retrieved polarization angle on the sky of magnitude $2\,\overline{\beta}_{ea} = 10$–$15°$ (3–5°) at 250 (500) μm. The 350 μm band, however, is minimally perturbed by this effect.

In principle, the measured Mueller matrix can be used to generate a synthetic time-ordered template of the polarization modulation produced by the HWP as if it were continuously rotated at a mechanical frequency $f = \omega t$. Continuous rotation of the HWP allows the rejection of all the noise components modulated at harmonics different than $4f$ (synchronous demodulation) and is typically employed by experiments optimized to measure the polarization of the CMB (e.g. Johnson et al. 2007; Reichborn-Kjennerud et al. 2010). In such experiments, the HWP modulation curve leaves a definite synchronous imprint on the time-ordered bolometer data streams, hence it is of utter importance to characterize the template and remove it from the raw data. However, a time-ordered HWP template would be of no use to a step-and-integrate experiment such as BLASTPol, whose timelines are not dominated by the HWP synchronous signal.

We have measured the phase shift of the HWP across the wavelength range of interest to be within 5° of the ideal 180° for the central BLASTPol band, and within 15° for the side bands. This is due to a combination of alignment errors of the sapphire substrates, which are hard to avoid in the manufacture of a five-slab stack, and their lower than ideal thickness. However, the modulation efficiency of the HWP is only mildly affected by this departure from ideality, being above 98 per cent in all three BLASTPol bands. Moreover, departures of similar amplitude are not uncommon for HWPs at (sub)mm wavelengths.

The goal of the second part of this work was to include the measured non-idealities of the HWP as-built in a map-making algorithm. We have focused on the implementation of a naive binning technique for the case of BLASTPol, under the assumption of white and uncorrelated noise. As a proof of concept, we have presented a preliminary polarization map for one of the scientific targets observed by BLASTPol during its first Antarctic flight, completed in 2011 January. The inferred direction for the local magnetic field in the Carina Nebula star-forming region is in excellent agreement with the results obtained by Li et al. (2006) with the SPARO instrument. The empirical approach presented in this paper will help improve the accuracy on astronomical measurements of the polarization angle on the sky at submm wavelengths.

ACKNOWLEDGEMENTS

The BLASTPol collaboration acknowledges the support of NASA through grant numbers NAG5-12785, NAG5-13301 and

NNGO-6GI11G, the Canadian Space Agency (CSA), the Science and Technology Facilities Council (STFC), Canada's Natural Sciences and Engineering Research Council (NSERC), the Canada Foundation for Innovation, the Ontario Innovation Trust, the Puerto Rico Space Grant Consortium, the Fondo Institucional para la Investigacion of the University of Puerto Rico, the National Science Foundation Office of Polar Programs and the Canadian Institute for Advanced Research.

REFERENCES

Ade P. A. R., Pisano G., Tucker C., Weaver S., 2006, in Zmuidzinas J., Holland W. S., Withington S., Duncan W. D., eds, Proc. SPIE Conf. Ser., Vol. 6275, Millimeter and Submillimeter Detectors and Instrumentation for Astronomy III. SPIE, Bellingham, p. 62750U
Ade P. A. R. et al., 2011, A&A, 536, A1
Bao C. et al., 2012, ApJ, 747, 97
Bastien P., Bissonnette É., Ade P., Pisano G., Savini G., Jenness T., Johnstone D., Matthews B., 2005, J. R. Astron. Soc. Can., 99, 133
Benoît A. et al., 2004, A&A, 424, 571
Bernard J.-P. et al., 2007, EAS Publ. Ser., 23, 189
Blain A. W., 1999, MNRAS, 304, 669
Blain A. W., Barnard V. E., Chapman S. C., 2003, MNRAS, 338, 733
Brown M. L., Challinor A., North C. E., Johnson B. R., O'Dea D., Sutton D., 2009, MNRAS, 397, 634
Bryan S. A., Montroy T. E., Ruhl J. E., 2010a, Appl. Opt., 49, 6313
Bryan S. A. et al., 2010b, in Holland W. S., Zmuidzinas J., eds, Proc. SPIE Conf. Ser., Vol. 7741, Millimeter, Submillimeter, and Far-Infrared Detectors and Instrumentation for Astronomy V. SPIE, Bellingham, p. 7741H
Cantalupo C. M., Borrill J. D., Jaffe A. H., Kisner T. S., Stompor R., 2010, ApJS, 187, 212
Chandrasekhar S., Fermi E., 1953, ApJ, 118, 113
Collett E., 1993, Polarized Light: Fundamentals and Applications. Marcel Dekker, New York
Cook W. B., Perkowitz S., 1985, Appl. Opt., 24, 1773
Crutcher R. M., 2004, Ap&SS, 292, 225
Crutcher R. M., 2012, ARA&A, 50, 29
Crutcher R. M., Troland T. H., Lazareff B., Paubert G., Kazès I., 1999, ApJ, 514, L121
Crutcher R. M., Nutter D. J., Ward-Thompson D., Kirk J. M., 2004, ApJ, 600, 279
Davis L., Jr, Greenstein J. L., 1951, ApJ, 114, 206
Dolginov A. Z., Mitrofanov I. G., 1976, Ap&SS, 43, 291
Dowell C. D. et al., 2010, in McLean I. S., Ramsay S. K., Takami H., eds, Proc. SPIE Conf. Ser., Vol. 7735, Ground-based and Airborne Instrumentation for Astronomy III. SPIE, Bellingham, p. 77356H
Fissel L. M. et al., 2010, in Holland W. S., Zmuidzinas J., eds, Proc. SPIE Conf. Ser., Vol. 7741, Millimeter, Submillimeter, and Far-Infrared Detectors and Instrumentation for Astronomy V. SPIE, Bellingham, p. 77410E
Greaves J. S. et al., 2003, MNRAS, 340, 353
Hanany S., Hubmayr J., Johnson B. R., Matsumura T., Oxley P., Thibodeau M., 2005, Appl. Opt., 44, 4666
Hildebrand R. H., 1983, Q. J. R. Astron. Soc., 24, 267
Hildebrand R. H., Dragovan M., Novak G., 1984, ApJ, 284, L51
Hildebrand R. H., Davidson J. A., Dotson J. L., Dowell C. D., Novak G., Vaillancourt J. E., 2000, PASP, 112, 1215
Houde M., Vaillancourt J. E., Hildebrand R. H., Chitsazzadeh S., Kirby L., 2009, ApJ, 706, 1504
Johnson B. R. et al., 2007, ApJ, 665, 42
Kennaugh E. M., Adachi S., 1960, IEEE Trans. Microw. Theory Tech., 8, 520
Lazarian A., 2007, J. Quant. Spectrosc. Radiat. Transfer, 106, 225
Li H., Griffin G. S., Krejny M., Novak G., Loewenstein R. F., Newcomb M. G., Calisse P. G., Chuss D. T., 2006, ApJ, 648, 340
Li H., Dowell C. D., Kirby L., Novak G., Vaillancourt J. E., 2008, Appl. Opt., 47, 422
Loewenstein E. V., Smith D. R., Morgan R. L., 1973, Appl. Opt., 12, 398
Marsden G. et al., 2008, in Duncan W. D., Holland W. S., Withington S., Zmuidzinas J., eds, Proc. SPIE Conf. Ser., Vol. 7020, Millimeter and Submillimeter Detectors and Instrumentation for Astronomy IV. SPIE, Bellingham, p. 702002
Martin D. H., Puplett E., 1970, Infrared Phys., 10, 105
Masi S. et al., 2006, A&A, 458, 687
Matsumura T., Hanany S., Ade P. A. R., Johnson B. R., Jones T. J., Jonnalagadda P., Savini G., 2009, Appl. Opt., 48, 3614
Matthews T. G. et al., 2013, preprint (arXiv:1307.5853)
McKee C. F., Ostriker E. C., 2007, ARA&A, 45, 565
Moncelsi L., 2011, PhD thesis, Cardiff University, UK, available at: http://orca.cf.ac.uk/13144/
Murray A. G., Nartallo R., Haynes C. V., Gannaway F., Ade P. A. R., 1997, in Wilson A., ed., ESA SP-401: The Far Infrared and Submillimetre Universe. ESA, Noordwijk, p. 405
Natoli P., de Gasperis G., Gheller C., Vittorio N., 2001, A&A, 372, 346
Natoli P., Botti M., de Gasperis G., De Troia G., Massaioli F., 2009, Mem. Soc. Astron. Ital. Suppl., 13, 84
Novak G., Gonatas D. P., Hildebrand R. H., Platt S. R., 1989, PASP, 101, 215
Novak G. et al., 2003, ApJ, 583, L83
O'Dea D., Challinor A., Johnson B. R., 2007, MNRAS, 376, 1767
O'Dea D. T. et al., 2011, ApJ, 738, 63
Pancharatnam S., 1955, Mem. Raman Res. Inst. Bangalore, 71, 137
Pascale E. et al., 2008, ApJ, 681, 400
Pascale E. et al., 2011, MNRAS, 415, 911
Pascale E. et al., 2012, in Stepp L. M., Gilmozzi R., Hall H. J., eds, Proc. SPIE Conf. Ser., Vol. 8444, Ground-based and Airborne Telescopes IV. SPIE, Bellingham, p. 844415
Patanchon G. et al., 2008, ApJ, 681, 708
Pisano G., Savini G., Ade P. A. R., Haynes V., Gear W. K., 2006, Appl. Opt., 45, 6982
Pisano G., Savini G., Ade P. A. R., Haynes V., 2008, Appl. Opt., 47, 6251
Press W. H., Teukolsky S. A., Vetterling W. T., Flannery B. P., 1992, Numerical recipes in C: The Art of Scientific Computing, 2nd edn. Cambridge Univ. Press, New York
Reichborn-Kjennerud B. et al., 2010, in Holland, Wayne S., Zmuidzinas Jonas., eds, Proc. SPIE Conf. Ser., Vol. 7741, Millimeter, Submillimeter, and Far-Infrared Detectors and Instrumentation for Astronomy V. SPIE, Bellingham, p. 77411C
Renbarger T. et al., 2004, PASP, 116, 415
Rex M., 2007, PhD thesis, Univ. Pennsylvania
Salatino M., de Bernardis P., Masi S., Polenta G., 2012, ApJ, 748, 1
Savini G., Pisano G., Ade P. A. R., 2006, Appl. Opt., 45, 8907
Savini G., Ade P. A. R., House J., Pisano G., Haynes V., Bastien P., 2009, Appl. Opt., 48, 2006
Soler J. D., Hennebelle P., Martin P. G., Miville-Deschênes M.-A., Netterfield C. B., Fissel L. M., 2013, ApJ, 774, 128
Stokes G. G., 1852, Ann. Phys., Lpz., 163, 480
Title A. M., Rosenberg W. J., 1981, in Giorgio B. T., ed., Proc. SPIE Conf. Ser., Vol. 307, Polarizers and Applications. SPIE, Bellingham, p. 120
Truch M. D. P., 2007, PhD thesis, Brown University
Ward-Thompson D., Kirk J. M., Crutcher R. M., Greaves J. S., Holland W. S., André P., 2000, ApJ, 537, L135
Whittet D. C. B., Hough J. H., Lazarian A., Hoang T., 2008, ApJ, 674, 304
Wiebe D. V., 2008, PhD thesis, Univ. Toronto, Canada
Wootten A., Thompson A. R., 2009, Proc. IEEE, 97, 1463
Wu J. H. P. et al., 2007, ApJ, 665, 55
Zhang J., Ade P. A. R., Mauskopf P., Moncelsi L., Savini G., Whitehouse N., 2009, Appl. Opt., 48, 6635
Zhang J., Ade P. A. R., Mauskopf P., Savini G., Moncelsi L., Whitehouse N., 2011, Appl. Opt., 50, 3750

This paper has been typeset from a TEX/LATEX file prepared by the author.